Article

The International Journal of Robotics Research
2017, Vol. 36(4) 414–435

DOI: 10.1177/0278364917706743
journals.sagepub.com/home/ijr
SAGE

An upper-body rehabilitation exoskeleton Harmony with an anatomical shoulder mechanism: Design, modeling, control, and performance evaluation

Bongsu Kim and Ashish D Deshpande

Abstract

We present an upper-body exoskeleton for rehabilitation, called Harmony, that provides natural coordinated motions on the shoulder with a wide range of motion, and force and impedance controllability. The exoskeleton consists of an anatomical shoulder mechanism with five active degrees of freedom, and one degree of freedom elbow and wrist mechanisms powered by series elastic actuators. The dynamic model of the exoskeleton is formulated using a recursive Newton–Euler algorithm with spatial dynamics representation. A baseline control algorithm is developed to achieve dynamic transparency and scapulohumeral rhythm assistance, and the coupled stability of the robot–human system at the baseline control is investigated. Experiments were conducted to evaluate the kinematic and dynamic characteristics of the exoskeleton. The results show that the exoskeleton exhibits good kinematic compatibility to the human body with a wide range of motion and performs task-space force and impedance control behaviors reliably.

Keywords

Upper-body exoskeleton, robotic rehabilitation, shoulder mechanism, scapulohumeral rhythm, dynamic modeling, series elastic actuator

1. Introduction

Neuromuscular insults, such as a stroke or a spinal cord injury, affect a substantial portion of the US population, resulting in significant disabilities (Centers for Disease Control and Prevention, 2009; Go et al., 2014). For instance, approximately 80% of all stroke survivors experience some form of upper limb paresis, with only 18% of those gaining full motor recovery within the following year (Combs et al., 2010; Rijntjes et al., 2009; Wing et al., 2008). To date, a number of robotic devices have been developed for the upper extremity that have provided promising rehabilitation outcomes (Kahn et al., 2006; Kwakkel et al., 2008; Prange et al., 2006; Volpe et al., 2001). Still, the success of robotic systems in delivering therapy after a neurological disorder is limited (Byl et al., 2013; Klamroth-Marganska et al., 2014; Lo et al., 2010; Milot et al., 2013).

A robotic exoskeleton worn around the upper body has the potential to control the human joints for coordinated movements. One key design challenge is powering the movements of the shoulder complex through its full range without discomfort to the user. The natural movements of the upper arm are strongly coordinated with the movements of the shoulder girdle, represented by the scapulohumeral rhythm (SHR). To achieve the full range of upper-body movements, the shoulder girdle must be powered synergistically with the upper arm. Without attention to the coordinated motion at the shoulder, joint instability may occur, resulting in shoulder pain or injuries including irritation and impingement of the rotator cuff (Dromerick et al., 2008). Also, since the coordinated motion is a key functionality of the shoulder girdle and is a natural consequence of serial actuation by muscles running from the thorax to the humerus via the shoulder girdle, it may be beneficial to include this coordinated motion in the rehabilitation process of the upper limb for effective clinical results (Jaraczewska and Long, 2006).

A number of existing upper-body exoskeletons support the mobility of the glenohumeral (GH) joint, excluding that

The University of Texas at Austin, USA

Corresponding author:
Bongsu Kim, The University of Texas at Austin, 204 East Dean Keeton Street, Austin, TX 78712, USA.
Email: bskim@utexas.edu

of the shoulder girdle (Garrec et al., 2008; Klein et al., 2008; Perry et al., 2007; Tsagarakis and Caldwell, 2003; Vertechy et al., 2009). These exoskeletons typically attach to the user's hand or wrist but not to the upper arm. NO connection at the upper arm makes the robots less sensitive to the kinematic incompatibility around the shoulder, thus allowing for simplicity in robot design. Exoskeletons with a connection at the upper arm are beneficial in assisting upper limb motion with proper coordination at the shoulder. However, careful attention is required in kinematic design to match with the anatomical structure, including the shoulder girdle, for minimizing undesirable residual force to the human joints.

Some exoskeletons are designed to partially support the mobility of the shoulder girdle: either elevation–depression (Carignan et al., 2005; Nef et al., 2009) or protraction–retraction (Sanchez et al., 2005). Another design idea is to support shoulder girdle movements either with passive joints (Stienen et al., 2009; Taal and Sankai, 2011) or with a combination of passive and active joints (Ergin and Patoglu, 2012; Ren et al., 2009). These systems comply with the full mobility of user-driven shoulder girdle movements with the advantage of self-alignment. The presence of passive joints, however, can limit active assistance to the shoulder girdle mobility. An exoskeleton for telemanipulations with a six degree of freedom (6-DOF) end-effector connected to the upper arm also allows for full mobility of the shoulder (Schiele and van der Helm, 2006); but this idea has not been evaluated for rehabilitation applications where higher forces are usually required. One exoskeleton design supports both elevation and protraction with a two degree of freedom (2-DOF) mechanism that characterizes the kinematics of the shoulder girdle (Ball et al., 2007). However, this idea has only been presented conceptually. Also, its bulky shoulder mechanism possibly limits an extension to a bi-manual design with a wide range of motion (ROM) because of the interferences between the left- and right-hand sides of the shoulder mechanisms during bilateral abduction. Bilateral training is considered as an important part of upper-body rehabilitation, enhancing the rehabilitation efficacy depending on the clinical condition of patients (Cauraugh et al., 2010; Stewart et al., 2006; Waller and Whitall, 2008; Whitall et al., 2000).

Many studies suggest that the voluntary effort of patients during therapeutic movements facilitates the relearning process of the lost motor function (Conditt et al., 1997; Krakauer, 2006; Lee et al., 1994; Schmidt and Lee, 1988).To encourage voluntary movements of patients, exoskeletons need to be dynamically transparent as much as possible to let patients take over the task when they can. Dynamic transparency requires robots to have a good performance in force and impedance control, relying on the minimum impedance that robots can achieve (Krebs et al., 1998). The ability to control force and impedance is also beneficial for implementing novel therapeutic interventions and providing a safe interaction environment. However, few upper-body exoskeletons employ force and impedance-oriented actuators, such as series elastic actuators (SEAs).

In this paper, we present a bi-manual upper-body exoskeleton, called Harmony, with an anatomical shoulder mechanism that provides a natural mobility around the shoulder with a wide ROM and SEAs that allow good force and impedance control. With a dynamic model, a baseline control is developed for the robot to exhibit a high dynamic transparency and to perform good task-space force and impedance control. The following sections present the hardware design, kinematic and dynamic modeling, control design and stability analysis, and experimental evaluation of the upper-body exoskeleton.

2. Human shoulder kinematics for exoskeleton design

The versatile mobility of the upper extremity is partly due to a wide ROM of the GH joint and a synergetic movement between the upper arm and shoulder girdle known as the SHR. The SHR results in translational motions of the GH joint, such as elevation–depression and protraction–retraction. Usually, the mobility of the GH joint is realized by a ball-and-socket joint mechanism in exoskeletons. When the upper arm is attached to the counterpart of an exoskeleton, the center of rotation (COR) of the ball-and-socket joint mechanism must follow the translational motions of the GH joint for kinematic compatibility between the human body and the exoskeleton. To characterize the translational motions of the GH joint, we recorded the trajectory of the acromion of a healthy subject that is located right above the GH joint, during repetitive shoulder elevation–depression and protraction–retraction using a motion capture system (PhaseSpace, Inc.). The markers were attached on the sternum, sternoclavicular (SC) joint, and acromion.

The experimental results show that the trajectory of the GH joint falls in circular arcs (Figure 1). Therefore, it is possible to translate the ball-and-socket joint by a linkage that supports pivot motions with respect to the centers of rotation of the circular arcs.

The results also indicate that the COR of elevation–depression and protraction–retraction in the shoulder girdle motion shifts away from the SC joint. This shift probably occurs when the distance between the GH joint and the SC joint is reduced as muscle contraction around the shoulder girdle increases during shoulder elevation or protraction. As a result, the curvature of the trajectory is deformed and this leads to the shifting of the center of the approximated circle. Constraints from ligaments around the SC joint are also partly responsible for shifting the COR away from the SC joint (Levangie and Norkin, 2011). The amount of shifting and shortening may vary across individuals by their body size and flexibility around the shoulder. To support the shifted COR with the shortened radius, a shoulder girdle mechanism requires an adjustable location of the pivot point and a link with an adjustable length.

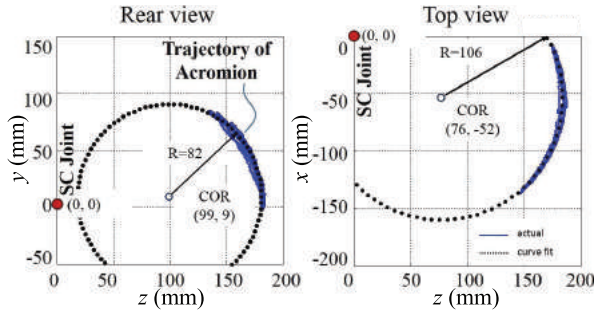

Fig. 1. The trajectory of the acromion during the right-hand shoulder girdle motion of a healthy subject: (a) elevation–depression; (b) protraction–retraction. Axes x, y, and z are aligned with the sagittal, longitudinal, and frontal axis, respectively. SC: sternoclavicular; COR: center of rotation.

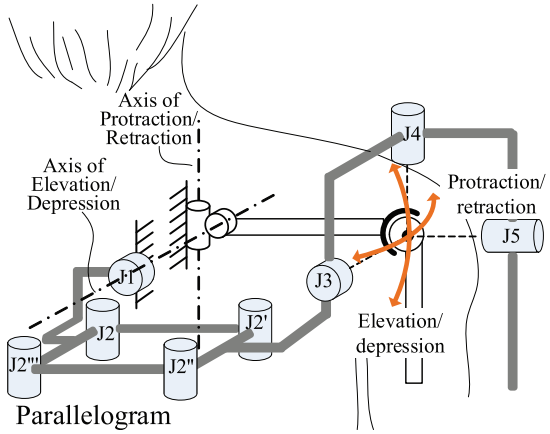

Fig. 2. Schematic view of a shoulder girdle mechanism combined with a parallelogram.

The pivot motion of the clavicle, in other words, SC motion, consists of elevation–depression, protraction–retraction, and anterior–posterior axial rotation. The mobility of anterior–posterior axial rotation of the clavicle can be safely ignored during the design of the shoulder girdle mechanism, because the functionality of anterior–posterior axial rotation widens the ROM of the GH joint but does not add another degree of freedom.

3. System design

3.1 Shoulder girdle mechanism

A ball-and-socket joint is kinematically equivalent to a serial chain with three rotational joints whose axes intersect at a single point. When the serial chain is placed alongside the shoulder, kinematic compatibility requires that the intersection point of the serial chain co-locates with the COR of the GH joint during the shoulder girdle movements. Based on the observation in Figure 1, we designed a shoulder girdle mechanism that consists of a revolute joint and a parallelogram (Figure 2). The revolute joint, $J1$ in Figure 2, duplicates the mobility of the shoulder elevation and depression, and the parallelogram, $J2$ $J2'$ $J2''$ $J2'''$, duplicates the mobility of the shoulder protraction and retraction.

The parallelogram may be substituted with a revolute joint that is located above the head to coincide with the axis of protraction and retraction of the human shoulder, but this configuration restricts the ROM of bi-manual abduction because of the possible collision between the revolute joints at both sides. The revolute joint may also be located in the anterior side of the shoulder near the COR of the protraction and retraction, but the mechanism in front of the shoulder likely reduces the ROM of the arm near the torso. When the revolute joint lies at the back of the shoulder, an offset of the COR of the protraction–retraction causes major kinematic discrepancy.

The parallelogram resolves the kinematic discrepancy that would be created if a revolute joint were adopted for the protraction and retraction at the backside of the shoulder. The parallelogram shifts the circular motions with respect to the axis of the revolute joint at the backside into those with respect to the axis of the protraction and retraction of the human shoulder (Figure 2). Consequently, the shoulder girdle mechanism provides kinematically compatible mobilities for protraction–retraction and elevation–depression while securing the ROM of the upper limb.

3.2 Ball-and-socket joint

Three revolute joints that are perpendicularly arranged with each other are usually adopted in the ball-and-socket joint of upper-body exoskeletons. To enhance the ROM while avoiding mechanical singularities and interferences with the human body, our ball-and-socket joint consists of three revolute joints that are arranged with an acute angle, as shown in Figure 3. Accordingly, the joint at the top of the shoulder, $J4$, is aligned to the vertical axis with an angle outwards and backwards. In addition, axis $J3$ is aligned to the sagittal axis $x - x$ with an angle outwards, so that joint $J4$ is leaning toward the back side of the shoulder during shoulder abduction and avoids collision with the shoulder or the head. For design simplicity, the orientation of joint $J5$ at the default pose with relaxed arms points in the direction of the transverse axis $z - z$. Angles α, β, and γ are determined based on the shape and volume of the actuators on the joint, and on the trade-off between a large abduction angle and the avoidance of singularity. Figure 4 shows an example of the relationship between those angles, the ROM, and the singularity. When angles α and β are smaller, axis $J4$ lies further outwards and backwards from the shoulder, where more clearance is ensured between $J4$ and the shoulder at high abduction angles (Figure 4(a)) and between $J4$ and the upper arm at high forward flexion angles (Figure 4(b)). However, a smaller angle restricts the

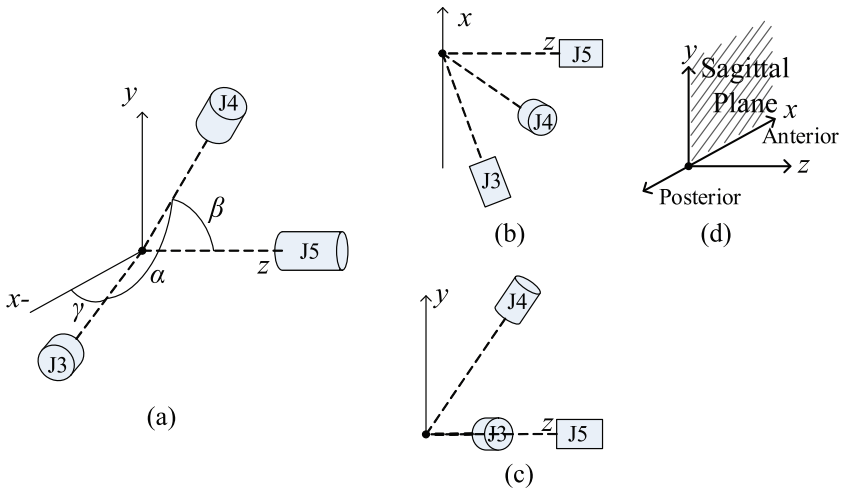

Fig. 3. The optimized mechanism for the glenohumeral joint in the right-hand shoulder: (a) isometric view; (b) top view; (c) rear view; (d) plane definition.

ROM of the arm posed in front of the torso (Figure 4(c)). A larger angle of γ in Figure 3 secures more clearance for axis $J4$ during the abduction, but the larger angle limits the range of external rotation because of the interference or singularity between joints $J3$ and $J5$ (Figure 4(d)). With the angles between the axes, the distance between the intersecting point and each joint also affects the ROM. In particular, the ROM of bilateral abduction is mainly limited by a collision between both sides of $J4$, which is facilitated by the increased angle of $J1$ during the coordinated motion of the shoulder girdle mechanism. The ROM of unilateral abduction is mainly limited by the interference between $J4$ and the ipsilateral shoulder. A higher position of $J4$ increases the angle where the interference in the unilateral abduction occurs, but reduces the angle where the collision in the bilateral abduction occurs.

The interactions between the complex surfaces of the human body, actuator units, and linkages are impossible to model accurately, making it difficult to use a numerical optimization technique. So, we used a number of three-dimensional (3D) printed mock-ups to determine the parameter values for the mechanism that results in a large ROM. In the Harmony design, the angles α, β, and γ were set to be 60°, 60°, and 18°, respectively.

3.3 Forearm mechanism

To support rotational motion along the longitudinal axis in the body segment, such as pronation and supination of the forearm, we developed a new mechanism with a light and compact structure. In many wearable robots, such rotational motions are generated by a curved rail bearing (Perry et al., 2007) surrounding the arm segments. However, this bearing is generally bulky and heavy, and could possibly restrict the ROM of the arm in a situation where the arm moves close to the torso. Figure 5 shows our new mechanism, which generates the same motion with a curved linear bearing. This mechanism consists of a parallelogram and a transmission that transfers the rotation of the link in the parallelogram to the handle. Pulley 1 rotating with the link in the parallelogram drives the timing belt connecting pulley 2. Pulley 2 is grounded via a bearing to the branch extruding from the other link in the parallelogram. Then, a handle or a wrist mechanism attached to pulley 2 revolutes along a circular path and simultaneously spins about the axis of pulley 2. The transmission can be either a timing belt, a gear train, or an auxiliary parallelogram, as long as it delivers the same rotational direction with a 1-to-1 gear reduction ratio. This mechanism is potentially light and easy to build. Another mechanism for supporting rotation along the longitudinal axis has been presented previously (Stienen et al., 2009), but the underlying kinematics of our design are distinct, resulting in a more compact structure.

3.4 Final kinematic design and alignment

In the final kinematic design of the shoulder mechanism (Figure 6), joints $J3$, $J4$, and $J5$, consisting of the ball-and-socket joint, are arranged at an oblique angle to each other, thus increasing the ROM while avoiding the mechanical singularity within the workspace of the upper limb. The ball-and-socket joint connects the shoulder girdle mechanism, consisting of one revolute joint $J1$ and a parallelogram $J2$, which translates the ball-and-socket joint along the trajectory of shoulder protraction–retraction and elevation–depression. The distance between both sides of $J1$ and the length of the link in the parallelogram are adjustable to match shoulder size and the radius of the shoulder girdle motion. The upper arm and forearm segments are also adjustable for a wide range of subject body dimensions.

Alignment between the robot and the human body is important, since misalignment causes undesirable stress on the skeleton and joints. The COR of the ball-and-socket joint matches that of the GH joint in terms of three parameters: ‘a’ the elevation of the shoulder mechanism; ‘b’ the distance between both sides of $J1$; and ‘c’ the gap between

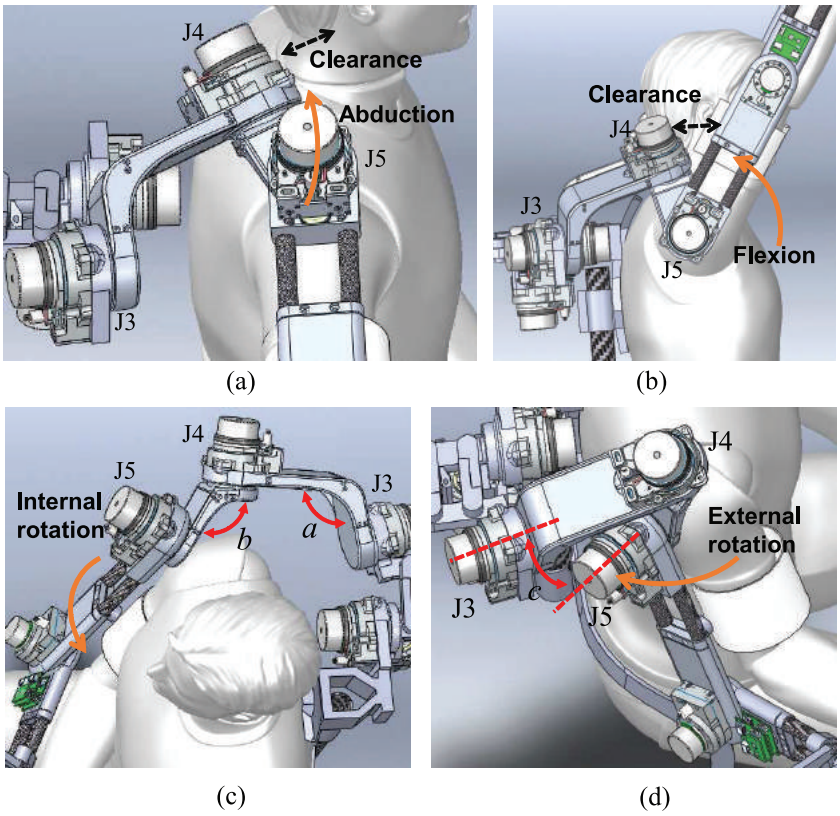

Fig. 4. The three degree of freedom ball-and-socket joint. An oblique arrangement of joint $J4$ provides a clearance with the head during abduction (a), and also a clearance with the upper arm during forward flexion (b). The larger the values of angles a and b (smaller α and β in Figure 3), the smaller the range of motion of the internal rotation due to the singularity among $J3$, $J4$, and $J5$ (c). In the case of very large γ in Figure 3 (less margin at angle c), the range of motion of the external rotation is limited by the interference or singularity between joints $J3$ and $J5$ (d).

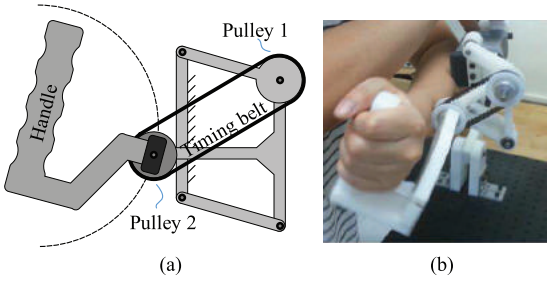

Fig. 5. A new mechanism for supporting pronation and supination of the forearm: (a) the kinematic diagram; (b) the prototype of the mechanism.

the back and the shoulder mechanism. Adjustment for parameters 'a' and 'c' is relatively straightforward if a therapist recognizes the COR of the GH joint by palpation and visual observation. The shoulder width is also easily adjustable by fitting both sides of the upper arm cuff to the body. However, the ratio between the length of the parallelogram and the subject's shoulder width needs to be investigated through a human subject study. For example, around 60% of the distance between the SC and acromioclavicular joints was acceptable for a good kinematic compatibility throughout a number of individuals in our trials. Using such a ratio, adjustment of shoulder width and parallelogram length can be done by one-time measurement of the subject's shoulder dimension. The adjusting mechanism in the current system is realized by a sliding mechanism with a lock, but a quick adjustment mechanism may need to be developed to reduce the setup time in the clinical application. With the current setup, it takes around 10 minutes to adjust all the link lengths on both arms and around 3 minutes more to wear the robot.

The adjustment process requires one to measure the subject's body size, including shoulder width and sitting height, at the beginning of rehabilitation process. The torso of a hemiparetic patient is usually lopsided, and both sides of the shoulders are unleveled. So, body size measurement needs to be done carefully for hemiparetic patients. The torso needs to be fixed with respect to the ground of the shoulder mechanism for alignment, and a harness is required to support the torso.

3.5 Actuation type

Rehabilitation robots frequently provide force- or impedance-based therapeutic trainings, such as impedance-based

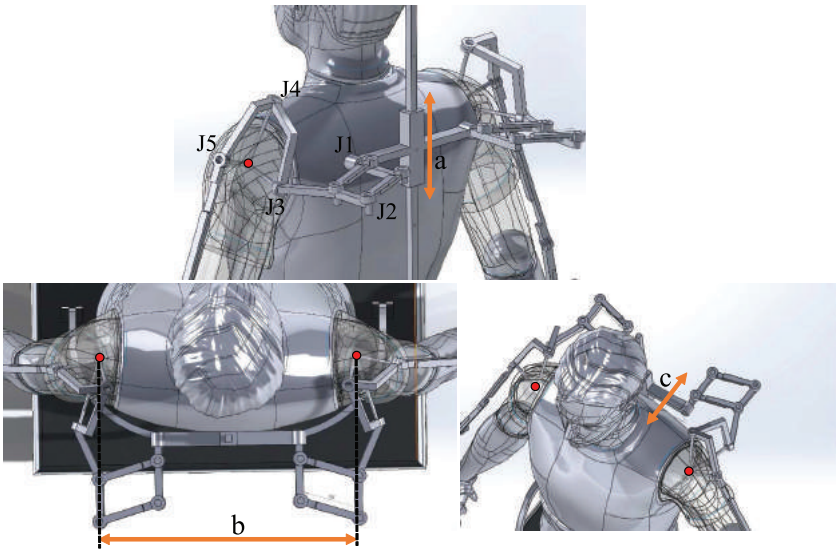

Fig. 6. The final kinematic design of the shoulder mechanism. The three adjustment parameters a, b, and c allow one to align the center of rotation of the *ball-and-socket joint* with that of the subject's glenohumeral joint.

Table 1. Specifications of Harmony.

List	Value
Continuous torque	34.4 N·m @ shoulder 13 N·m @ elbow 1.25 N·m @ wrist
Torque bandwidth	7 Hz
Backdrivability	Less than 0.3 N·m @ 0.6 rad/s
Robot weight	31.2 kg excluding the frame
Control frequency	Up to 2000 Hz

resistant exercises (Andreasen et al., 2004) and force field-based trainings (Banala et al., 2007; Patton et al., 2006). For example, robots with force control can render an aquatic therapy-like environment with an active gravity compensation for the weight of the robot and the full or partial weight of users while allowing user-driven free motions with or without viscous-like resistance (Kong et al., 2010). We selected SEAs to implement various force- and impedance-based therapeutic exercises, because a SEA offers precise and stable force control with robustness to impulsive disturbances (Pratt et al., 1995) and is capable of producing a very low impedance (Zinn et al., 2004), which is essential to encourage users' voluntary movements.

3.6 Fully constructed system

Figure 7 shows the final computer-aided design (CAD) of Harmony and the constructed system. The robot is equipped with SEAs at all 14 axes, linkages with an adjustable length, and four multi-axis force/torque sensors at the interaction ports of the wrist and upper arm. A wrist cuff and handle are commonly grounded at the force/torque sensor in the wrist. A chest harness attached to the frame is used to support the torso. Each actuator is a compact rotary SEA designed previously (Edsinger-Gonzales and Weber, 2004) and modified with a torque-type brushless direct current (DC) motor (Maxon Motor, EC Flat series) and a Harmonic Drive (Harmonic Drive LLC). Specifications, including continuous torque of the SEA, appear in Table 1.

The robot is operated by a real-time control system running Linux patched with RT-Preempt (Figure 8). The customized motor drivers run the motor of the SEA, communicating with the Linux system via EtherCAT. A server program on the Linux system manages the EtherCAT communication with all motors and sensors, and low-level controls such as torque control. The server program runs simultaneously with a C++ code that contains a high-level control by communicating via a shared memory interface.

Safety is ensured with emergency stop buttons for the user and the operator and also by hard stops at every joint. Additional safety features are added at the software level to limit the ROM, avoid self-collision, limit joint velocity, and stop the robot at an excessive interaction force/torque.

4. Modeling of Harmony

In order to develop a control algorithm involving a feed-forward torque that compensates for the robot dynamics, we formulated an inverse dynamic model of the robot. We present a methodology for modeling kinematics and dynamics of the robot that includes the unconventional parallelogram joint and adjustable-length body segments. Before modeling the robot dynamics, we first formulate the actuator dynamics to examine the SEA of Harmony as a torque source, since our control system is separated into two layers, robot-level and actuation-level controls.

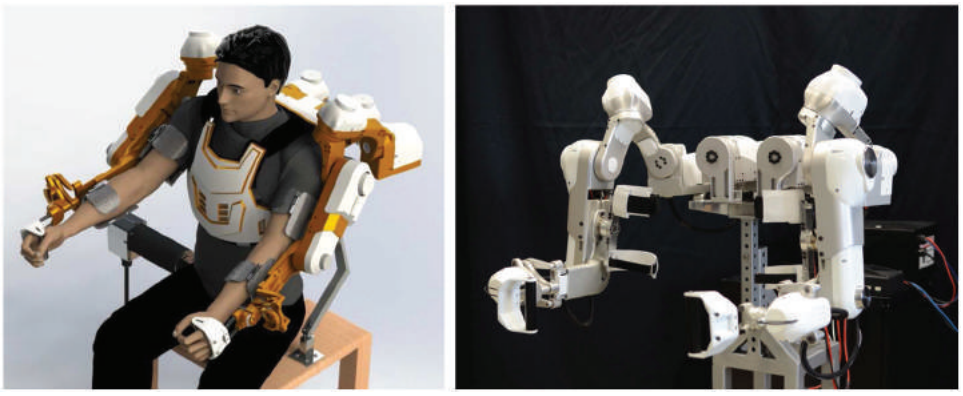

Fig. 7. Upper-body exoskeleton Harmony.

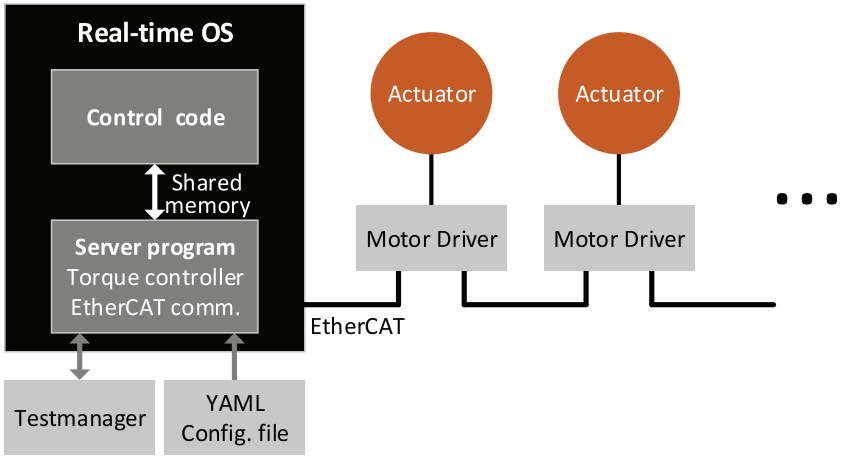

Fig. 8. The software platform controlling the upper-body exoskeleton. A graphical user interface (Testmanager from EtherLab®) to visualize parameters and a C++ environment is available. A YAML file is used to configure parameters at the start of the server program. OS: operating system.

4.1 Dynamics of SEA

Proportional–integral–derivative (PID) control with feedback from the spring deflection is used to control the torque output of the SEA. However, the deflection of the spring does not directly measure the actual torque output of the SEA in a non-steady state because the SEA adopts a configuration in which a spring lies between the stator of the motor and the ground, as illustrated in Figure 9(a), where the dynamics of the motor stator also affect the torque output. Nevertheless, this configuration is advantageous to mechanical construction and sensor placement, because the spring and sensor for detecting spring deflection can be grounded (Paine et al., 2014). Figure 9(b) shows an analogically equivalent mechanical system of the SEA. The compliance and the mass of the stator unit of the SEA are analogous to those of the fulcrum of the level system. At a static equilibrium, the deflection of the spring directly indicates the output torque, but movement of the masses in the input and the fulcrum adds dynamic forces to the torque output.

The dynamics of the rotor and the stator of the motor are as follows

$$J_m(\ddot{\theta}_{m/s} + \ddot{\theta}_s) + C_m\dot{\theta}_{m/s} + f_{hd} + \tau_{ml} = \tau_m \quad (1)$$

$$J_s\ddot{\theta}_s + K_{se}\theta_s = (N+1)\tau_{ml} - \tau_m \quad (2)$$

$$N\tau_{ml} = \tau_o \quad (3)$$

$$\theta_{m/s} = N(\theta_s - \theta_o) \quad (4)$$

where θ_s and θ_o represent the displacement of the stator and output shaft with respect to the ground, respectively, and $\theta_{m/s}$ is the relative displacement of the rotor with respect to the stator. The rotation of the output of the Harmonic Drive is in the opposite direction to that of the input. Motor torque τ_m delivers a load torque τ_{ml} to the Harmonic Drive, overcoming the acceleration of the rotor with moment of inertia J_m, damping C_m, and friction f_{hd} of the gear from the motor input side. The load torque (τ_{ml}) amplified by gear ratio N is transferred to the output τ_o while accelerating the stator unit J_s and deforming the

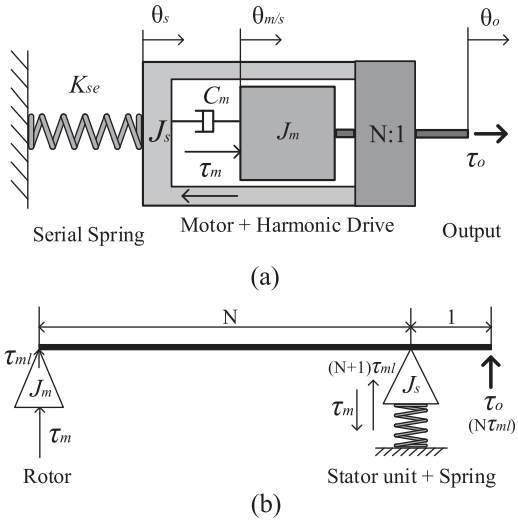

Fig. 9. The flipped configuration of the series elastic actuator: (a) illustration of the series elastic actuator; (b) equivalent mechanical system.

spring with stiffness K_{se}. When the output shaft is fixed $(\theta_o = 0)$, the output torque can be expressed as

$$\tau_o = -(J_{eq}\ddot{\theta}_s + C_{eq}\dot{\theta}_s + f_{hd} + K_{se}\theta_s) \tag{5}$$

where J_{eq} and C_{eq} are the equivalent moment of inertia and damping coefficient for the rotor and the stator unit, respectively. The negative sign of the torque is due to the opposite directional output of the Harmonic Drive in equation (5). The dynamic forces of the motor unit and the friction (f_{hd}) of the Harmonic Drive at the input side appear in the SEA output because of the SEA's spring configuration, where the motor is grounded via the spring. In controlling the motor of the SEA, the effects of the motor dynamics and the friction are considerable compared with the magnitude of the motor torque and they largely affect the control performance. However, the torque from the dynamic terms that appeared in equation (5) might be small compared to that of the spring torque $(K_{se}\theta_s)$, especially at low frequencies. In that case, the spring torque $(K_{se}\theta_s)$ can be approximated as the SEA output (τ_o), simplifying the output measurement. The comparison between the spring torque and the SEA output will be shown in Section 6.

4.2 Forward and inverse kinematics of the shoulder mechanism

The shoulder mechanism contains a parallelogram, which is a multi-link structure but still has one degree of freedom. So, a parallelogram can be treated as a joint with one joint variable. However, a parallelogram is not defined as a joint, such as a revolute or prismatic joint, in conventional robotic kinematics; therefore, we need to define forward and inverse kinematics across the parallelogram. The oblique arrangement of the ball-and-socket joint also complicates the calculation of inverse kinematics. To address these problems, we have developed a methodology that involves attaching frames and performing coordinate transformations across the parallelogram and the ball-and-socket joint.

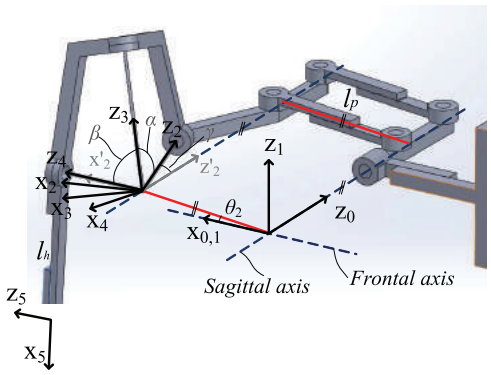

Fig. 10. The coordinate representation of the kinematics of the shoulder mechanism. The ith axis (z_{i-1}) is aligned to joint Ji and frame 0 is grounded. Axis x_2 of frame 2 locates at the center of rotation of the ball-and-socket joint instead of at the common normal of axis z_1 and z_2. The values of α, β, and γ are 60, 60, and 18 degrees, respectively.

Figure 10 shows the coordinate representation of the shoulder mechanism. For the simplicity of calculation and angle representation, coordinate 2 is placed at the center of the ball-and-socket joint. This is a deviation from the standard Denavit–Hartenberg (DH) convention (Paul, 1981) with which coordinate 2 would be off the COR of the ball-and-socket joint, while the other coordinates follow the DH convention. In this case, a rotational transformation with respect to axis $y_{2'}$ by angle γ is added to transform coordinate 2 to the intermediate coordinate system of $x_{2'}$, $y_{2'}$, and $z_{2'}$, which is attached to the third link of the parallelogram where axis z_2 is connected. Table 2 represents the DH parameters and the intermediate coordinate transformation for coordinate 2′.

The kinematics of a parallelogram are different from those of a revolute joint. The rotation of a parallelogram changes position but not orientation of the following linkage. The transformation between frames 2 and 1 is as follows

$$^1P = \begin{bmatrix} 1 & 0 & 0 \\ 0 & c\alpha_2 & -s\alpha_2 \\ 0 & s\alpha_2 & c\alpha_2 \end{bmatrix} {}^{2'}P + \begin{bmatrix} c\theta_2 & -s\theta_2 & 0 \\ s\theta_2 & c\theta_2 & 0 \\ 0 & 0 & 1 \end{bmatrix} \begin{Bmatrix} l_p \\ 0 \\ 0 \end{Bmatrix} \tag{6}$$

$$^{2'}P = \begin{bmatrix} c\gamma & 0 & s\gamma \\ 0 & 1 & 0 \\ -s\gamma & 0 & c\gamma \end{bmatrix} {}^2P \tag{7}$$

^iP represents the position of point P with respect to coordinate i. Transformation of the others axes is expressed as

$$^{i-1}P = \begin{bmatrix} c\theta_i & -s\theta_i & 0 \\ s\theta_i & c\theta_i & 0 \\ 0 & 0 & 1 \end{bmatrix} \left(\begin{bmatrix} 1 & 0 & 0 \\ 0 & c\alpha_i & -s\alpha_i \\ 0 & s\alpha_i & c\alpha_i \end{bmatrix} {}^iP + \begin{Bmatrix} a_i \\ 0 \\ d_i \end{Bmatrix} \right) \tag{8}$$

Table 2. Denavit–Hartenberg parameters and the rotation for the intermediate transformation for coordinate 2.

i	a_i	d_i	α_i	θ_i
1	0	0	-90	θ_1 (variable)
$2'$	l_p	0	-90	θ_2 (variable)
2	Rotation with respect to $y_{2'}$ by γ			
3	0	0	$-\alpha$	θ_3 (variable)
4	0	0	β	θ_4 (variable)
5	l_h	0	0	θ_5 (variable)

Therefore, the rotational and position transformation from coordinates 5 to 0 can be expressed as

$$ {}^0_5R = Z_{\theta_1}X_{\alpha_1}X_{\alpha_2}Y_\gamma Z_{\theta_3}X_{\alpha_3}Z_{\theta_4}X_{\alpha_4}Z_{\theta_5}X_{\alpha_5} \tag{9} $$

$$ {}^0P = {}^0_5R({}^5P + [l_h\ 0\ 0]^{\mathrm{T}}) + Z_{\theta_1}X_{\alpha_1}Z_{\theta_2}[l_p\ 0\ 0]^{\mathrm{T}} \tag{10} $$

${}^0_5R$ is the total rotational matrix from coordinates 5 to 0. Z_{θ_i} and X_{θ_i} represent the rotational matrix with respect to z_i and x_i by angle θ_i and α_i, respectively. The intermediate transformation, Y_γ, is a rotation matrix with respect to $y_{2'}$ by angle γ for the transformation between frames 2 and $2'$. ${}^0P$ and ${}^5P$ are the position vectors with respect to coordinates 0 and 5, respectively. Note that there is no rotational transformation by angle θ_2 in the total rotational matrix. The rotation by angle θ_2 (rotation in the parallelogram) affects only the positional calculation in equation (10).

Inverse kinematics for the shoulder mechanism convert the origin and the angle of coordinate 5 into the angles of the joints

$$ {}^0O_5 - {}^0_5R[l_h\ 0\ 0]^{\mathrm{T}} = {}^0O_{2,3,4} = Z_{\theta_1}X_{\alpha_1}Z_{\theta_2}[l_p\ 0\ 0]^{\mathrm{T}} \tag{11} $$

$$ Y_\gamma^{\mathrm{T}}X_{\alpha_2}^{\mathrm{T}}X_{\alpha_1}^{\mathrm{T}}Z_{\theta_1}^{\mathrm{T}}{}^0_5R = Z_{\theta_3}X_{\alpha_3}Z_{\theta_4}X_{\alpha_4}Z_{\theta_5}X_{\alpha_5} \tag{12} $$

${}^0O_5$ and ${}^0_5R$ are the position of the origin and the angle of coordinate 5, respectively, and are the known values for an inverse kinematics problem. The left-hand side of equation (11) indicates the position of the COR of the ball-and-socket joint (the origin of coordinate 2, 3, 4) with respect to the fixed frame. Since origin ${}^0O_{2,3,4}$ is a known vector, $\theta_{1,2}$ on the right-hand side of equation (11) can be calculated from the three equations of the vector components. With the values of θ_1 and θ_2 known, θ_3,θ_4, and θ_5 can be calculated by equation (12).

4.3 Inverse dynamics

The unconventional arrangement of the parallelogram joints and adjustable-length links in Harmony make it difficult to utilize general dynamic libraries. Instead, in this study we formulate the dynamic model using a recursive Newton–Euler method with spatial dynamics representation, which provides efficient calculation suited for a real-time control environment (Featherstone and Orin, 2000). The inverse dynamic modeling process consists of kinematic recursion and force recursion. Kinematics are calculated through forward recursion from the base to the end-effector of a robot, expressed as

$$ {}^0\hat{v}_i = {}^0\hat{v}_{i-1} + {}^0\hat{s}_i\dot{\theta}_i \tag{13} $$

$$ {}^0\hat{a}_i = {}^0\hat{a}_{i-1} + {}^0\hat{\dot{s}}_i\dot{\theta}_i + {}^0\hat{s}_i\ddot{\theta}_i \tag{14} $$

where ${}^0\hat{v}_i$, ${}^0\hat{a}_i$, and ${}^0\hat{s}_i$ are 6×1 spatial vectors of the velocity, acceleration, and joint axis, respectively. The left-hand superscript of the parameters refers to the reference frame, and frame '0' indicates an inertial reference frame. The right-hand subscript is the link and joint number in ascending order from the base link to the end-effector and the hat indicates spatial quantities. Feed-forward torques are calculated through backward recursion, expressed as

$$ {}^0\hat{f}_i = {}^0\hat{f}_{i+1} + {}^0\hat{I}_i{}^0\hat{a}_i + {}^0\hat{v}_i \hat{\times} {}^0\hat{I}_i{}^0\hat{v}_i \tag{15} $$

$$ \tau_i = {}^0\hat{s}_i \hat{\cdot} {}^0\hat{f}_i \tag{16} $$

where ${}^0\hat{f}_i$, ${}^0\hat{I}_i$, and ${}^0\tau_i$ are the 6×1 spatial force, 6×6 spatial inertia matrix, and scalar joint torque or force, respectively. $\hat{\times}$ and $\hat{\cdot}$ express spatial the cross and dot product, details of which can be found in Featherstone (1987).

4.3.1 Task-space force and impedance. From equation (13), the spatial velocity of the *n*th link can be expressed in a matrix form as

$$ {}^0\hat{v}_n = \left[{}^0\hat{s}_1 \cdots {}^0\hat{s}_n\right]\{\dot{\theta}_1 \cdots \dot{\theta}_n\}^{\mathrm{T}} \tag{17} $$

$$ {}^0\hat{J}_n = \left[{}^0\hat{s}_1 \cdots {}^0\hat{s}_n\right] \tag{18} $$

and the concatenation of the spatial joint vectors is the Jacobian $({}^0\hat{J}_n)$ of the transformation between the robot's joint velocities and the spatial velocity of the *n*th link. From the virtual work principle between joint space and task space, the static equilibrium between external spatial force ${}^0\hat{f}_e$ applied at the *n*th link and the joint torques from '1' to '*n*' is given as

$$ \tau^{\mathrm{T}} = {}^0\hat{J}_n{}^{\mathrm{T}}\begin{bmatrix} 0_3 & I_3 \\ I_3 & 0_3 \end{bmatrix}{}^0\hat{f}_e \tag{19} $$

or

$$ \tau_i = {}^0\hat{s}_i \hat{\cdot} {}^0\hat{f}_e \tag{20} $$

where τ and τ_i are the joint torque vector and scalar, respectively, and i runs from '1' to 'n'.

To apply a desired force or impedance at the interaction port attached on the *n*th link in task space, the velocity of the interaction port needs to be calculated from the spatial velocity of the link, which is obtained from equation (13), and the desired force needs to be converted into the spatial form to be used in equation (20). When point P is attached at the *n*th link and point O is the origin of the local reference frame of the link, the velocity of point P is given by

$$ {}^0v_P = {}^0v_O - OP \times {}^0\boldsymbol{\omega} \tag{21} $$

$$ {}^0\hat{v}_n = \left[{}^0\boldsymbol{\omega}^{\mathrm{T}}\ {}^0v_o{}^{\mathrm{T}}\right]^{\mathrm{T}} \tag{22} $$

${}^0v_P$ is the velocity of point P with respect to the global reference frame. ${}^0\boldsymbol{\omega}$ and ${}^0v_O$ are the first and the last three components of spatial velocity ${}^0\hat{v}_n$ of the nth link, and are the angular velocity of the link and the linear velocity of point O with respect to the global reference frame, respectively. OP is the vector from point O to point P with respect to the global reference frame.

The transformation of an external force or moment into a spatial form is given by

$$ {}^0f_e = \left[{}^0\hat{s}_F\ {}^0\hat{s}_M\right][F\ M]^{\mathrm{T}} \tag{23} $$

where

$$ {}^0\hat{s}_F = \left[{}^0\boldsymbol{\omega}_F{}^{\mathrm{T}}\ \left({}^0\boldsymbol{\rho}_F \times {}^0\boldsymbol{\omega}_F\right)^{\mathrm{T}}\right]^{\mathrm{T}} \tag{24} $$

$$ {}^0\hat{s}_M = \left[\vec{0}^{\mathrm{T}}\ {}^0\boldsymbol{\omega}_M{}^{\mathrm{T}}\right]^{\mathrm{T}} \tag{25} $$

F and ${}^0\hat{s}_F$ are the magnitude of the external force and the spatial vectors that describe the line of action and the point of application of the external force, respectively. Similarly, M and ${}^0\hat{s}_M$ are the magnitude of the external moment and the spatial vectors that describe the line of action of the external moment, respectively. ${}^0\boldsymbol{\omega}$ and ${}^0\boldsymbol{\rho}$ are the direction vector of the line of action and the location vector of any point on the line of action, respectively.

4.3.2 Spatial joint vector of the parallelogram joint. Spatial dynamics combines linear and rotational dynamics into one expression and simplifies the overall modeling process and calculation. The spatial joint vector, which is a key parameter in the modeling process, defines the direction and location of a given axis. This has been well defined previously for a rotational and prismatic joint but not for a parallelogram. The spatial joint vector is derived in describing the spatial velocity of a rigid body that expresses the translation and rotational velocity of a rigid body completely with six elements. Spatial velocity is defined as the linear velocity of a point on a rigid body that is instantaneously coincident with the origin of a reference frame.

Although a parallelogram is a multi-link mechanism, it acts as a joint with a single degree of freedom, and the spatial velocity of its moving body can be derived. Figure 11 shows the decomposition of the spatial velocity of body B of the parallelogram. The spatial velocity of body B can be expressed as a combination of the spatial velocity of body B' caused by the angular motion in axis a and the spatial velocity that brings body B' to B, induced by the angular motion in axis b, where the two angular motions are opposite in direction with an identical

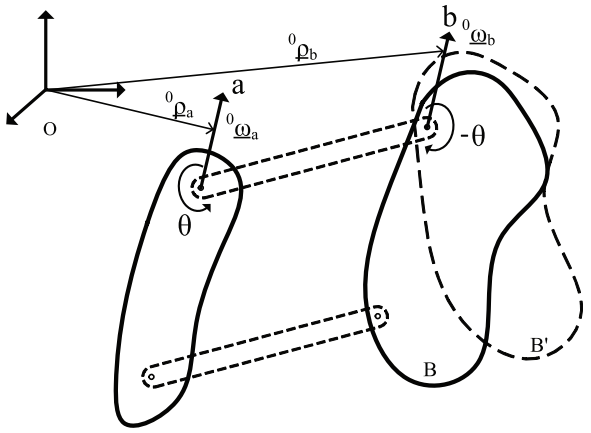

Fig. 11. Spatial joint vector for the parallelogram joint.

magnitude. Therefore, the spatial velocity of the parallelogram can be expressed as

$$ \begin{aligned} {}^0\hat{v}_B &= \begin{pmatrix} {}^0\boldsymbol{\omega}_a \\ {}^0\boldsymbol{\rho}_a \times {}^0\boldsymbol{\omega}_a \end{pmatrix}\dot{\theta} + \begin{pmatrix} {}^0\boldsymbol{\omega}_b \\ {}^0\boldsymbol{\rho}_b \times {}^0\boldsymbol{\omega}_b \end{pmatrix}(-\dot{\theta}) \\ &= \begin{pmatrix} \underline{0} \\ ({}^0\boldsymbol{\rho}_a - {}^0\boldsymbol{\rho}_b) \times {}^0\boldsymbol{\omega} \end{pmatrix}\dot{\theta} \\ &= {}^0\hat{s}_i\,\dot{\theta} \end{aligned} \tag{26} $$

where ${}^0\hat{v}_B$ is the spatial velocity of body B with respect to frame 0 and ${}^0\boldsymbol{\omega}_a$, ${}^0\boldsymbol{\rho}_a$, ${}^0\boldsymbol{\omega}_b$, ${}^0\boldsymbol{\rho}_b$ are the direction and location vectors of axes a and b with respect to frame 0, respectively. $\dot{\theta}$ and $-\dot{\theta}$ are the angular velocity in axes a and b, respectively. Since axes a and b are aligned in the same direction (${}^0\boldsymbol{\omega}_a = {}^0\boldsymbol{\omega}_b$), the spatial velocity of body B can be reduced to the form of ${}^0\hat{s}_i\dot{\theta}$ in equation (26). Therefore, ${}^0\hat{s}_i$ becomes the spatial joint vector of the parallelogram to be used in the modeling process.

4.3.3 Spatial inertia matrix of the adjustable-length link. Harmony consists of adjustable-length links for various body sizes. Determining the inertia matrix of an adjustable link with a complex 3D shape requires a calculation from a CAD software at every link length or it complicates the dynamic modeling process despite the parallel axis theorem in three dimensions. However, using spatial dynamics, the total inertial matrix of an adjustable-length link can be easily updated at variable lengths without an extra calculation, utilizing the feature of the spatial inertia matrix that supports arithmetic summation at a common coordinate frame

$$ {}^0\hat{I}_i = {}^0_{i1_c}\hat{X}\left({}^{i1_c}\hat{I}_{i1}\right){}^{i1_c}_0\hat{X} + {}^0_{i2_c}\hat{X}\left({}^{i2_c}\hat{I}_{i2}\right){}^{i2_c}_0\hat{X} \tag{27} $$

The 6×6 spatial inertia matrix of adjustable-length link 'i'(${}^0\hat{I}_i$) with respect to reference frame '0' is the sum of the spatial inertia matrices of the two consisting rigid bodies with respect to the same reference frame, as shown in equation (27). ${}^{i1_c}\hat{I}_{i1}$ and ${}^{i2_c}\hat{I}_{i2}$ are the two inertia matrices of the

two consisting bodies with respect to each local frame, '$i1_c$' and '$i2_c$', which are located at each center of mass and parallel to the local frame of link 'i'. The spatial inertia matrix is transformed by spatial transformation and its inverse transformation. ${}^{0}_{ij_c}\hat{X}$ is for transformation from frame 'ij_c' to '0' and is expressed as

$$ {}^{0}_{ij_c}\hat{X} = \begin{bmatrix} {}^{0}_{i}R & \mathbf{0}_{3\times 3} \\ \left({}^{0}r_{ij_c}\times\right){}^{0}_{i}R & {}^{0}_{i}R \end{bmatrix} \tag{28} $$

where ${}^{0}_{i}R$ is the rotational matrix from local frame 'i' to reference frame '0'. ${}^{0}r_{ij_c}$ is the location vector of the center of mass of body 'j' of link 'i' with respect to the reference frame, and is calculated as

$$ {}^{0}r_{ij_c} = {}^{0}r_i + {}^{0}_{i}R\,{}^{i}c_{ij} \tag{29} $$

where ${}^{0}r_i$ is the location vector of the origin of local frame 'i' with respect to the reference frame. ${}^{i}c_{ij}$ is the location vector of the center of mass of body 'j' of link 'i' with respect to local frame 'i' and contains the length value of the adjustable link. Therefore, by changing the value of the link length in ${}^{i}c_{ij}$, the spatial inertia matrix of adjustable-length link 'i' can be accordingly updated in the dynamic model.

5. Control for baseline behavior and stability analysis

5.1 Baseline control

For effective controls during rehabilitation intervention, our plan is to model the robot dynamics and then compensate for the weight and frictional forces of the robot, thus making the robot appear weightless and minimally resistive to the voluntary movements of patients. An assistive or resistive force, including gravity compensation for the patient body weight, then, can be added to this baseline behavior without major distortion from the robot dynamics.

Another component of the baseline behavior is the coupling torque for achieving the SHR. In rehabilitation practice for patients with an abnormal SHR, movements from the robot without a coordination with the shoulder girdle can cause pain, impingement, or injuries on the shoulder. Harmony's mechanism allows for powering of the SHR. We have developed an impedance controller that calculates the coupling torque for achieving the SHR (Kim and Deshpande, 2015). Using the reference angles of the shoulder girdle with respect to the angles of the upper arm, an impedance controller induces coordinated movements of the shoulder girdle. These movements are compliant to external disturbances, such as spasticity, to prevent injuries. Therapists might set the stiffness value in the impedance control to be small at the beginning of therapy for safety and increase the value depending on the patient's shoulder condition.

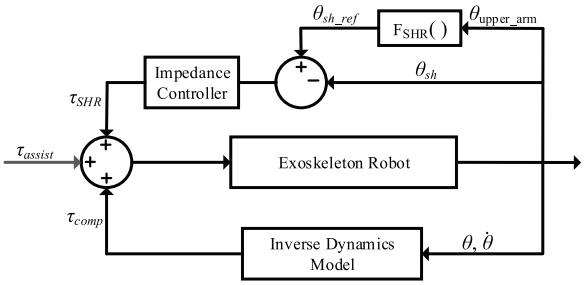

Fig. 12. Block diagram of the controller for baseline behavior of Harmony. Nonlinear function $F_{SHR}()$ calculates the reference position (θ_{sh_ref}) of the shoulder girdle mechanism from the angle of the upper arm (θ_{upper_arm}). $F_{SHR}()$ can be formulated from a curve fitting of data collected in the exoskeleton worn by healthy subjects.

Figure 12 shows the control block diagram to achieve baseline behavior of Harmony and equation (30) gives the controller terms

$$ M(\theta)\ddot{\theta} + C(\theta,\dot{\theta})\dot{\theta} + F\dot{\theta} + G(\theta) = \tau + \tau_I \tag{30} $$

$$ \tau = \tau_{comp} + \tau_{SHR} + \tau_{task} $$

$$ \tau_{comp} = \hat{G}(\theta) + f\dot{\theta} $$

$$ \tau_{SHR} = K_{sh}(\theta_{ref} - \theta) - D_{sh}\dot{\theta} $$

where $M(\theta)$, $C(\theta,\dot{\theta})$, F, and $G(\theta)$ are the inertia matrix, the Coriolis and centrifugal force matrix, the joint friction matrix, and the gravitational force vector, respectively. We assume that the joint friction is linear viscous damping and expressed as a positive definite diagonal matrix. τ and τ_I are the command torque and interaction torque between the robot and human, respectively. The interaction torque, τ_I, is the sum of the user–robot interaction forces (F_i) transformed by their corresponding Jacobians (J_i) at the interaction ports $(\tau_I = \sum J_i^{\mathrm{T}} F_i)$. τ_{comp} is a compensatory torque for gravity and joint friction, and $\hat{G}(\theta)$ is the estimated gravitational force vector. f is a friction compensation matrix of which elements are positive and smaller than the corresponding elements in the joint friction matrix. τ_{SHR} is the coupling torque that induces a normal SHR. K_{sh} and D_{sh} are the spring and damping coefficient matrices, respectively, where only the first and second diagonal components for the shoulder girdle joints are non-zero. The coupling torque can be set to zero when a patient does not need the SHR assistance. Assistive or resistive forces for therapeutic training are added to task torque τ_{task}, which is zero in the baseline behavior.

At the baseline behavior, a user can perform voluntary movements with minimal muscle effort that is just enough to overcome inertial, Coriolis and centrifugal forces, and residual frictional forces after the compensation. In robotic rehabilitation exercises, the arm movements are usually designed to be slow, where the effect from all dynamic terms is insignificant compared to that of gravity (Hollerbach and

Flash, 1982). In addition, the inertia forces of Harmony are further diminished because the SEA with its torque controller acts as a torque source and decouples the effect of the reflected inertia of the motor rotor (Vallery et al., 2008). With a zero-torque command, the torque controller tries to remove any spring deflection when the SEA output shaft is moved by a user. Since the torque controller in tracking the output shaft is much faster than the motion input by a user at a low frequency, the user does not feel the reflected inertia of the motor rotor because rotating the SEA output shaft does not directly accelerate the motor rotor. Still, some resistive torque can be produced during the backdrive due to the closed-loop system dynamics with respect to the motion input at the SEA output shaft. In our SEA, the resistive torque appears as the friction of a linear damping (which is presented in Section 6.3). However, the resistance is much lower than that from the reflected inertia, which usually produces a major portion of the inertia forces in a robot rigidly connected to high-ratio geared motors. For example, with a 120:1 gear ratio, the reflected inertia of the motor at the upper arm link of Harmony (Maxon EC 60 flat) is $1.728\ \mathrm{kg}\cdot\mathrm{m}^2$, while the upper arm link of Harmony has $0.158\ \mathrm{kg}\cdot\mathrm{m}^2$ of moment of inertia with respect to its rotational axis.

Compensating more for the residual forces may further enhance the dynamic transparency in the baseline control, but increase the possibility of violating stability criteria. Remaining frictional forces after the compensation are needed for maintaining the stability of the robot. By estimating acceleration from the joint position, a positive feedback to the torque input can compensate a part of the inertial force using the robot dynamics during user-driven free movements. However, inertia compensation can make the robot into a non-passive system that can jeopardize the coupled stability of the human–robot system when, for example, a user introduces a high stiffness by co-contractions (Kim et al., 2014). Also, an acceleration estimator introduces additional dynamics that can adversely affect the stability. Still, an investigation of the inertia compensation within a passive range in Harmony will be beneficial for dynamic transparency.

5.2 Stability of the baseline control

The coupled stability is fundamental to guarantee safety in the human–robot interaction system. The coupled stability of a human–robot system is guaranteed if the interacting port of the robot behaves passively, since the apparent dynamic behavior of the human limb is equivalent to that of a passive system (Colgate and Hogan, 1988; Hogan, 1989). To examine passivity at the baseline control, an energy storage function is formulated as the sum of the kinematic energy and the shaped potential energy as follows

$$V = \frac{1}{2}\dot{\theta}^{\mathrm{T}} M \dot{\theta} + \frac{1}{2}\tilde{\theta}^{\mathrm{T}} K_{sh} \tilde{\theta} \tag{31}$$

where V and M are the energy storage function and the inertia matrix of the robot, respectively. $\tilde{\theta}$ is the deviation of joint angles from their reference angles for the SHR assistance control, where only the first and second joint angles are used in the calculation. Having the control law as equation (30) with the assumption of $G(\theta) \simeq \hat{G}(\theta)$, the time derivative of the storage function at the baseline behavior is expressed as follows

$$\dot{V} = \dot{x}_I{}^{\mathrm{T}} F_I - \dot{\theta}^{\mathrm{T}}((F - f) + D_{sh})\dot{\theta} \tag{32}$$

where F_I and $\dot{x}_I$ are the vectors of the forces and velocities at the interaction ports, respectively. Power between the human $(\dot{x}_I{}^{\mathrm{T}} F_I)$ and the robot flows through the two interaction ports at each arm, and the combination of two subsystems with the dual ports for passivity formalism appears in Appendix 2. Equation (32) shows a passive mapping from human force F_I to velocity $\dot{x}_I$ at the interaction ports when $(F - f) + D_{sh}$ is positive definite. Before satisfying passivity, each joint has to be stable for human interaction safety. The friction compensation of each joint (f) needs to be smaller than the friction of the corresponding joint (F), which is the sum of the apparent friction of the controlled SEA and the friction of the robot joint after the SEA. Because of non-ideal factors in the torque control loop of the SEA, a positive feedback can compensate only a part of the joint friction. In our control, around 70% of the apparent friction of the SEA was compensated without the loss of stability (see Section 6.3). Also, each damping term of the SHR assistance in D_{sh} needs to be positive for the same reason. Since the condition for the individual joint stability is sufficient for the positive definiteness, the passivity mapping between the human and the robot holds. Once the robot is shown to be passive, the stability of the robot alone can be easily examined by having equation (31) as a Lyapunov candidate function and taking null of the human input. The time derivative of the function $(\dot{V} = -\dot{\theta}^{\mathrm{T}}((F - f) + D_{sh})\dot{\theta})$ is negative semi-definite, and the invariant set theorem with the radially unbounded Lyapunov function shows the robot with the baseline control to be globally asymptotically stable with the invariant set where $\dot{\theta} = 0$ with all θ (Slotine et al., 1991).

In practice, although the robot is controlled to be passive, the actual behavior may not be strictly passive, rather 'nearly' passive due to non-ideal factors such as actuator dynamics, model uncertainty, or time-delayed sensing and controlling. Such a nearly passive system can be destabilized when coupled with a rigid environment, which is usually referred to as the worst case (Chapel and Su, 1992). However, the soft actuators in Harmony increase the coupled stability margin because the combined stiffness in contact with a rigid environment is bounded by the compliance in the SEA (Kazerooni, 1987; Roberts et al., 1985).

6. Experiments with Harmony

We present the experimental procedure and results from two sets of experiments with Harmony: (i) firstly, to test

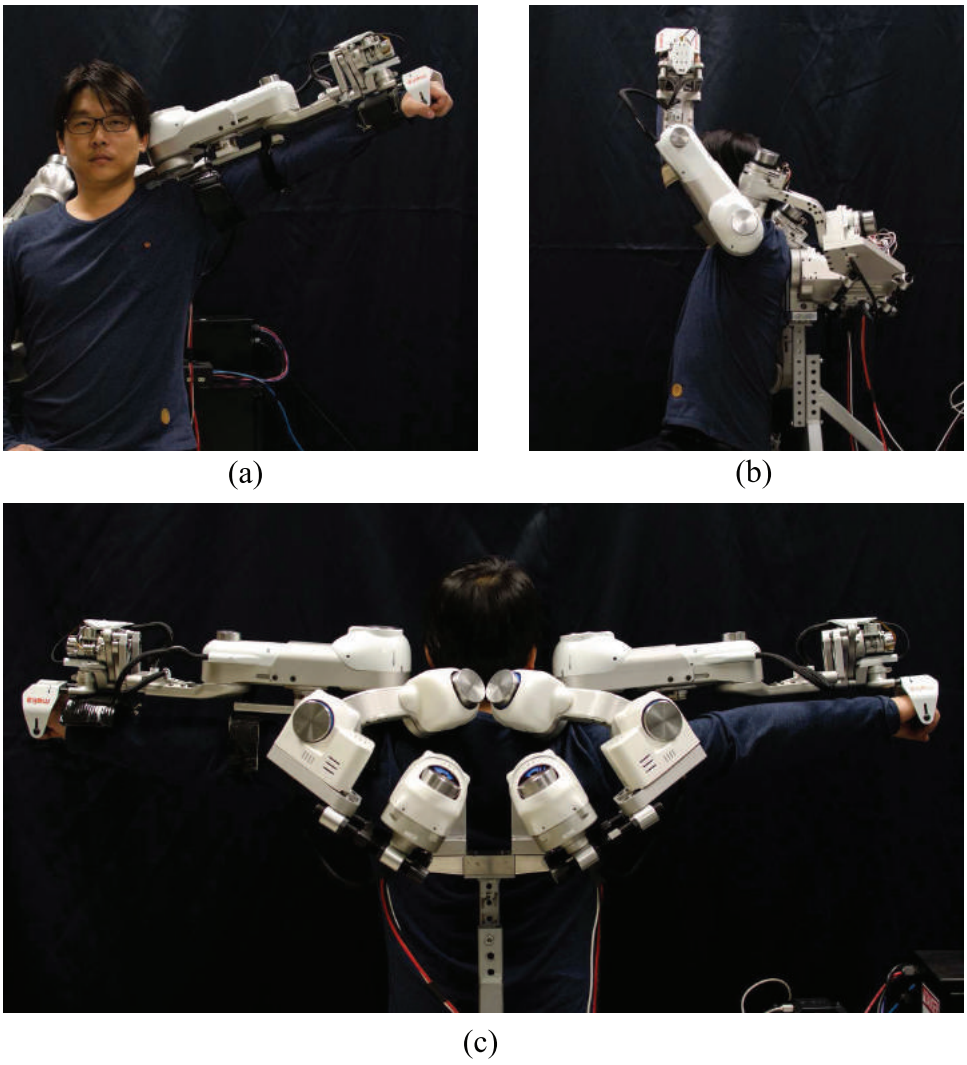

Fig. 13. Examples of the range of motion of the exoskeleton: (a) maximum abduction without external rotation. The range becomes larger with an external rotation, (b) maximum forward flexion, and (c) maximum bilateral abduction without external rotation where the range of motion is smaller than that of unilateral abduction because of the interference caused by the shoulder girdle mechanism. In all cases, humerothoracic elevation accompanies shoulder elevation.

and quantify the ROM of all the DOFs and test the kinematic compatibility around the shoulder, and (ii) secondly, to test dynamic performances of the robot. During both experiments, the baseline control was implemented.

6.1. Range of motion

In order to quantify the ROM, a user was asked to move the robot throughout its full possible range. The robot was connected to the user through the handle and the cuff at the upper arm. The cuff was securely connected to the upper arm at two points so that the robot followed the rotation and translation of the upper arm, including the shoulder girdle motion. Figure 13 shows several poses at the limits of the ROM. Figure 14 shows the range of 3D workspace of the left arm. The outer cloud of dots indicates the locations of the center of the wrist measured by the robot's position sensors during user-driven free movements. The inner small cloud of dots around the shoulder shows the locations of the COR of the ball-and-socket joint translated by shoulder protraction–retraction and elevation–depression during the free movements. The workspace covers almost the full ROM necessary for activities of daily living (ADLs), promising a sufficient ROM in therapeutic training (see Extension 1).

Table 3 compares the ROM of our robot with the mean values of the maximum ROMs of ADLs reported by Magermans et al. (2005). The ROM of the abduction is lower than that of ADLs due to the interference between $J5$ and the head; however, the abduction with external rotation offers a larger ROM, as does the human shoulder. The novel forearm mechanism also provides a ROM sufficient for pronation and supination. The two joints of the shoulder girdle mechanism have the ROM of 50° degrees in elevation, 5° in depression, 20° in protraction, and 45° in retraction. The ROM of each joint is restricted by a mechanical

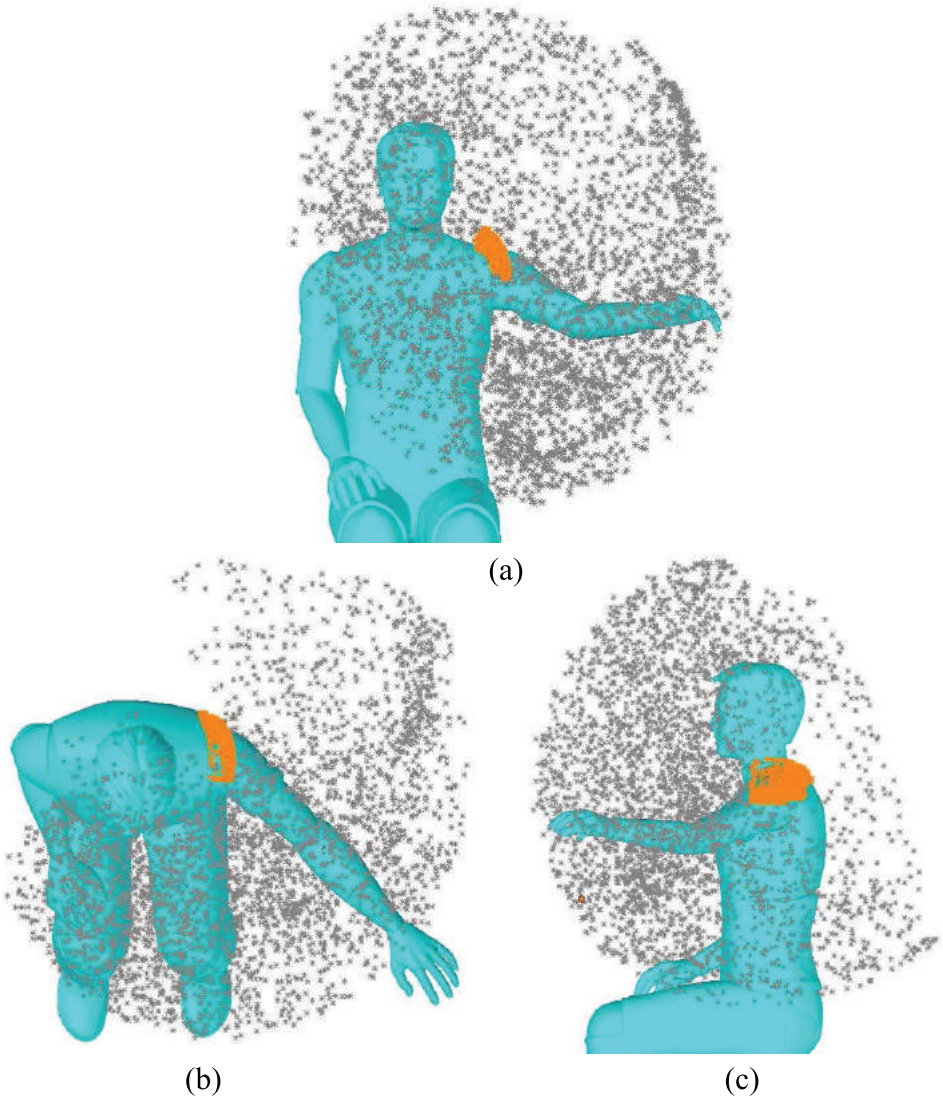

Fig. 14. Three-dimensional workspace of the end-effector (center of the wrist) measured by the robot's position sensors during free motion by a user wearing the robot in the baseline mode: (a) front view; (b) top view; (c) side view. The inner small point-cloud indicates the range of motion of glenohumeral joint translation.

hard stop for safety. During the bi-manual operation, the ROM of abduction in the absence of external rotation slightly decreases due to the interference of the shoulder mechanism itself (Figure 13(c)), but other shoulder motions maintain their wide ROM unless both arms interfere with each other.

6.2. Kinematic compatibility test

To evaluate the kinematic compatibility of the shoulder mechanism of Harmony, parasitic residual forces and torques at the upper arm interaction port were measured during humerothoracic elevation. The plane of elevation was selected to be around at 70° from the frontal plane where both shoulder protraction and elevation were recruited. To measure the interaction forces only from the kinematic discrepancy, the exoskeleton was under the baseline control with the SHR assistance off to ensure a high backdrivability and no forces were exerted by the robot weight or SHR control behaviors. Forces and torques were measured at several discrete positions during the user-driven humerothoracic elevation while the torso was fixed. The multi-axis force/torque sensor (ATI Industrial Automation, Mini 45) used for the measurement was attached between the robot upper arm link and cuff. The cuff is securely connected to the upper part and lower part of the human upper arm with two stiff rings consisting of inelastic straps and rigid semicircular shells covered by leathers. The stiff cuff is less

Table 3. Comparison between the measured range of motions (ROMs) of the robot and those of activities of daily living (ADLs) reported by Magermans et al. (2005). The value in the parentheses in 'Abduction' indicates the ROM of abduction with external rotation. In the case of external and internal rotation of the humerus, the maximum ROMs differ in accordance to arm configuration. The ROM of elbow flexion also moderately varies depending on the length of the forearm link. Values are in degrees.

Motion	ROM of the robot	ROM of ADLs
Abduction	118 (170)	131
Adduction	60	54.4
Forward flexion	160	130.5
Extension	45	50.5
External rotation	79 (62)	75.5
Internal rotation	80 (48)	61.7
Elbow flexion	150 (145)	148.1
Pro/supination	172	166.5

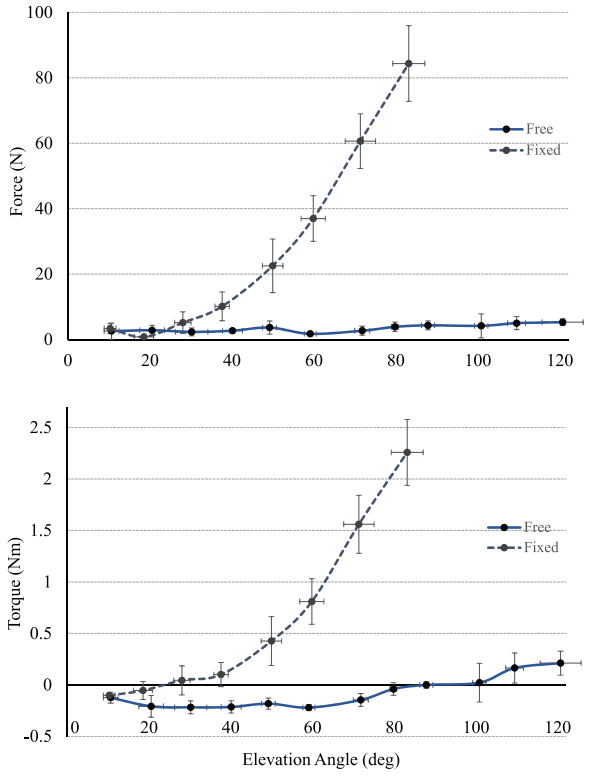

Fig. 15. Residual forces and torques exerted on the upper arm during shoulder humerothoracic elevation.

comfortable but provides a strict environment for evaluating the kinematic compatibility. The experiment was performed for two cases: (i) the shoulder girdle mechanism was free to move as designed; (ii) the shoulder girdle mechanism was locked, and for each case five trials were conducted.

Figure 15 shows the measured forces and torques in the two cases. The forces and torques with the full mobility in the shoulder mechanism remain very low during the elevation. The low values confirm the kinematic compatibility of the shoulder mechanism. In the case of fixed mobility in the girdle mechanism, the arm was impeded to elevate above 80° by the large interaction forces. Although the experiment were performed for the limited sets of ROMs, the tested motion evaluated the critical kinematic compatibility of the shoulder mechanism in supporting the natural shoulder mobility, including both shoulder protraction–retraction and elevation–depression, which is the key element of our design.

6.3. Joint-space torque responses

A preliminary torque controller adopts PD control based on the feedback from the deflection of the spring. The torque output at several low frequencies is shown in Figure 16 in the time domain. A chirp signal was fed into the torque command, and the frequency response was estimated from the output torque measured by the deflection of the spring. Figure 17 shows the Bode plot of the torque output, where the solid line is the torque measured by the spring and the dotted line is the actual torque estimated from equation (5). The difference between the measured torque and the actual torque is unnoticeable at a low frequency, so the torque measured by the spring can be considered as the torque output. The magnitude of the output torque is almost equal to that of the command up to around 10 rad/s, and resonance occurs around 45 rad/s (7 Hz).

The SEA exhibits low impedance behavior when the desired torque is set to zero in the torque controller. The impedance at the zero-torque command indicates the backdrivability in a joint level when a user moves the robot. To measure the joint backdrivability, a user was asked to rotate the output shaft of the SEA with various velocities. The position input and resistive torque were measured using the sensors of the SEA, while the velocity of the input motion was calculated in the post process using a high-order midpoint derivative after filtering.

The results show that the resistive torque during the backdriving movements is approximately linearly proportional to the input velocity, with 0.87 N · m/(rad/s) of friction coefficient (Figure 18). Therefore, the SEA can be considered as a combination of a pure torque source and apparent friction during backdriving movements. The backdrivability is mainly attributed to the performance of the torque controller in terms of the trackability of the motor position in canceling out the deflection of the SEA spring. To further enhance the backdrivability, while maintaining stability, a linear damping torque was positively fed back to the command input of the actuator to compensate for the part of the apparent friction of the SEA. The results in Figure 19 show that the backdrivability is enhanced with a reduced resistive torque. The resistive torque remains within 0.1 or 0.2 N · m, except a peak value at a moment when the direction of the movement is reversed. The joint velocity was conditioned using a first-order filter to reduce the noise from the derivative of the quantized position data.

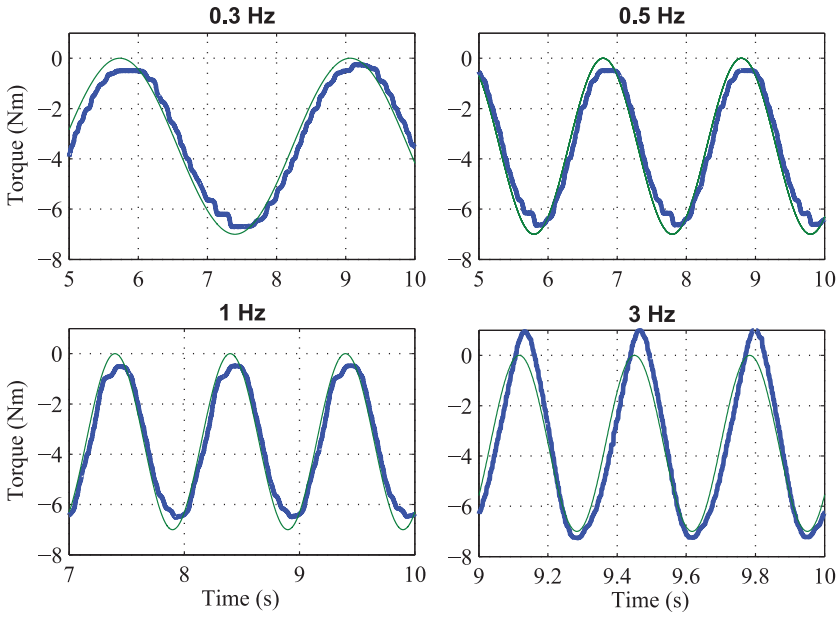

Fig. 16. Torque response of the series elastic actuator in the time domain with several frequencies of sinusoidal reference input. The light and heavy line indicate the commanded and actual torque, respectively. The force fidelities are 95.3%, 95%, 94.2%, and 92.3% at 0.3, 0.5, 1, and 3 Hz, respectively. The magnitude increases, as does the frequency.

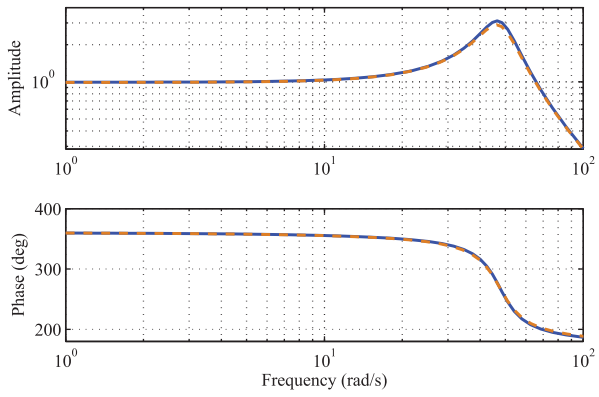

Fig. 17. Frequency response of torque control. The torque output measured by the deflection of the spring in the series elastic actuator (the solid line) is very close to the estimated actual torque output (the dotted line) at low frequency.

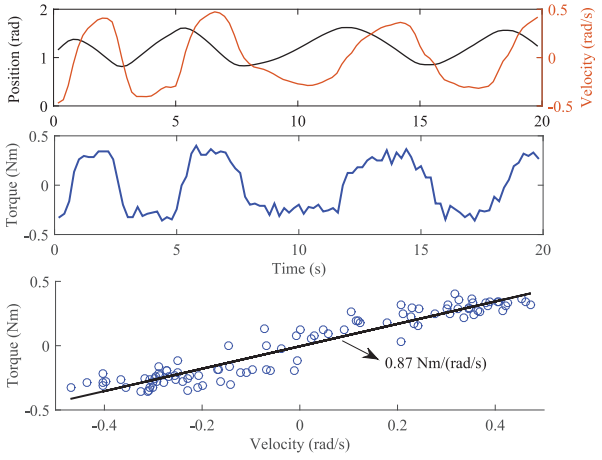

Fig. 18. Back-driving torque at the zero-torque command. With various velocities ranging from –0.5 to 0.5 rad/s, the resistive torque from the series elastic actuator ranges form –0.4 to 0.4 N · m with a strong tendency of linear viscous damping behaviors with 0.87 N · m/(rad/s) of friction coefficient.

6.4. Task-space force and impedance responses

To evaluate the performance of force and impedance control of the overall system, the robot was commanded to produce task-space forces and impedances at the interaction port located at the middle of the wrist. The last joint for the pronation–supination of the wrist was locked, leaving the arm to possess six degrees of freedom. A multi-axis force/torque load cell (ATI Inc., Nano 25) attached to the conjunction of the end-effector and the forearm link measured the forces, while the joint position sensors with the kinematic model measured the position and velocity of the interaction port. Figure 20 shows the robot configuration and the task-space coordinate system used in the experiments.

To measure force responses, reference forces were given to the command input while the end-effector was fixed to the ground. Figure 21 shows step force responses measured by the load cell at the wrist. The force outputs were filtered by a moving average with 10 Hz cutoff frequency. The rise time of the step response in each direction was around 22–24 ms for the rise from 0% to 100%. The maximum steady-state errors were around 10% at the commanded input of 5 N and 13% at the commanded input of 10 N. A force gauge (OMEGA, DFG55) was used to measure the steady-state errors and to offset the forces measured by the

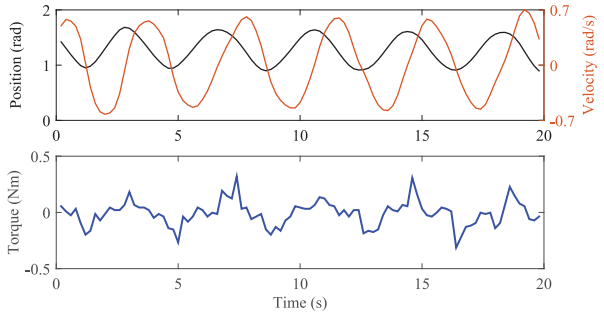

Fig. 19. Back-driving torque at the zero-torque command with friction compensation. Around 70% of the apparent frictional torque (0.6 N · m/(rad/s)) was positively fed back to the command input of the actuator.

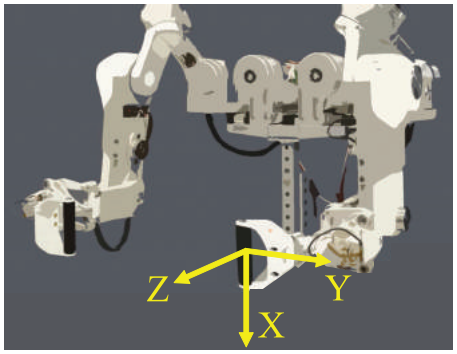

Fig. 20. Task-space coordinate system.

load cell, because the measurement by the load cell exhibited drifts and creeps. Figure 22 shows sinusoidal force responses. The time delay of the sinusoidal response was around 0.1 s, leading to 18 degrees of phase shift at 0.5 Hz input. The maximum amplitude error was around 13 % for the commanded amplitude of 8 N.

To evaluate impedance responses, reference forces corresponding to the position and velocity of the interaction port were given to the command input, and the interaction port was pulled along straight trajectories in the *Z*-direction.

The interaction port exhibits a minimum impedance behavior (see Extension 1) as an indication of backdrivability when the desired task-space force at the port is set to zero. Figure 23 shows an example of the backdrivability of the interaction port in the task space when a user slowly pulls the port back and forth. The resistive force was around 1–2 N with the peak value of around 2.5 N at the moment when the direction of the movement was reversed.

A spring-like behavior at the interaction port was implemented where the resistive force was proportional to the travel distance of the port from a reference point. The relationship between the force and the position with respect to the reference point exhibits close to linearity, and the effective stiffness values are estimated through a linear regression and exhibit around 11% error or less, as shown in Figure 24.

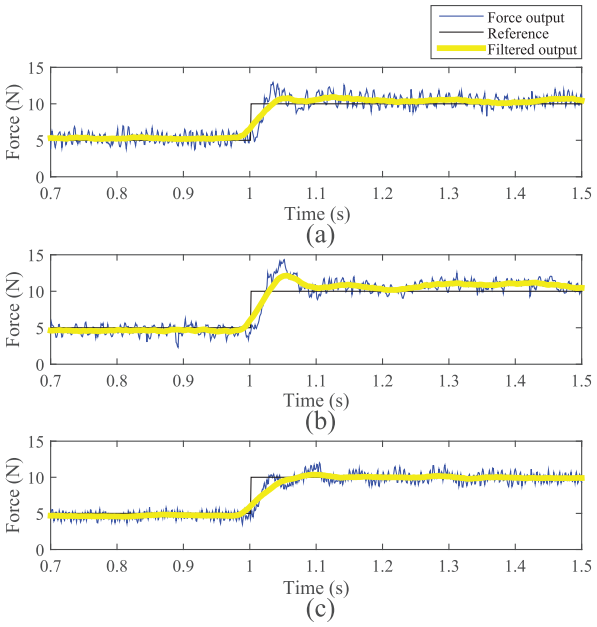

Fig. 21. Task-space step force responses with the rise from 5 to 10 N: (a), (b), and (c) are the step responses in the *X*, *Y*, and *Z*-directions in the task space, respectively.

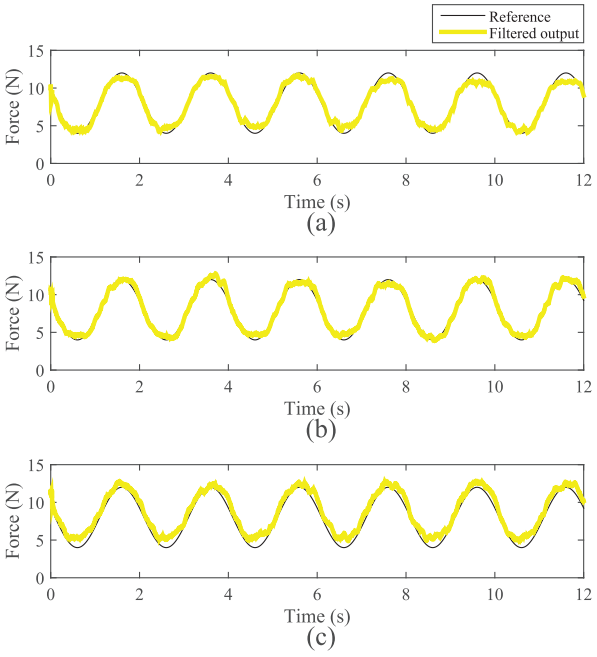

Fig. 22. Task-space sinusoidal force responses. The frequency of the reference input is 0.5 Hz with the magnitude from 4 to 12 N: (a), (b), and (c) are the sinusoidal responses in the *X*, *Y*, and *Z*-directions in the task space, respectively.

A damping-like behavior was implemented where the resistive force at the interaction port was proportional to the velocity of the port. The commanded damping coefficient was set to 100 N · s/m and a user pulled the interaction port back and forth in the *Z*-direction. The result in

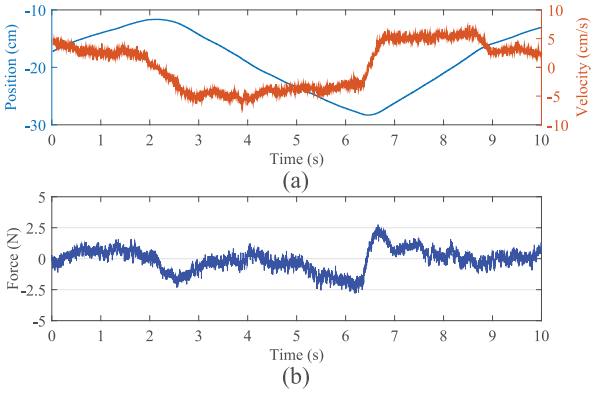

Fig. 23. Resistive forces at the interaction port when the command force input at the interaction port is set to zero and the port was pulled by a user in the *Z*-direction: (a) user-input position and velocity of the interaction port; (b) resistive forces with respect to time.

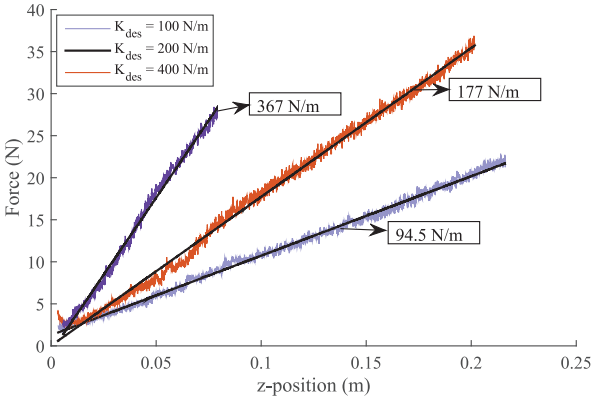

Fig. 24. Stiffness control responses at the interaction port in the *Z*-direction. The actual stiffnesses for the commanded values of 100, 200, and 400 N/m were 94.5, 177, and 367 N/m, respectively.

Figure 25 shows that the forces are correlated to the velocity with the coefficient of 0.96 and the effective damping coefficient exhibits around 5% error.

A trajectory control based on impedance was implemented for the interaction port to follow a linear trajectory back and forth repeatedly. The result shows that the interaction port follows the trajectory with a small deviation while allowing compliant behaviors to external disturbances (Figure 26).

Overall, the commanded task-space forces and impedances were reproduced across the 6-DOFs without a major distortion, promising various desired force and impedance behaviors for rehabilitation exercises to be designed. Although there were some response errors, the user could clearly feel the intended behaviors, including spring-like and damping-like behaviors. The errors in the task-space responses mainly originate from the error of the gravity compensation because of the parts, such as electric cables,

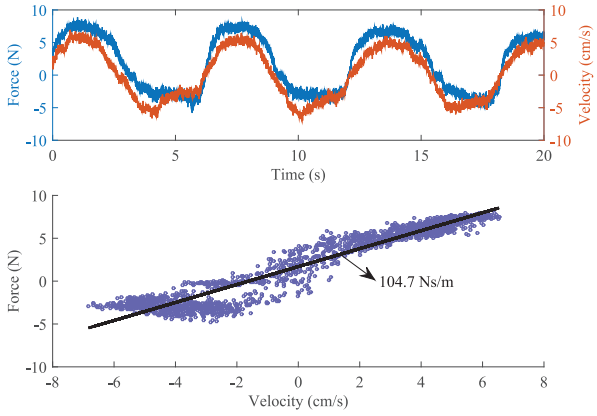

Fig. 25. Task-space damping-like behavior at the interaction port in the *Z*-direction. The commanded damping coefficient is 100 N · s/m.

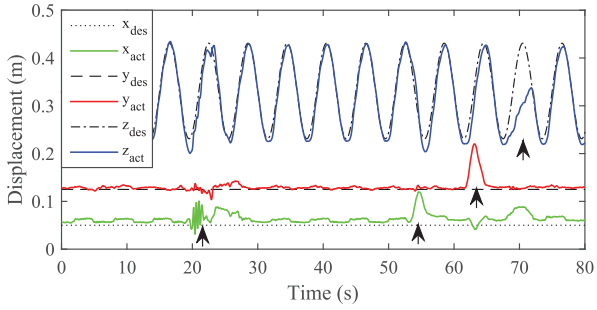

Fig. 26. Impedance-based tracking performance in task space and responses to external disturbances. The arrows indicate the points where external disturbances are applied.

that can not be precisely included in the CAD model because of the arbitrary shape and the error in the zero-set of the individual actuators, which can be improved in the future. Main source of noise in the data of the task-space experiment is the loadcell-type force sensor not the robot's behaviors, and users feel smooth reactive forces during the interaction with the robot.

7. Discussion

The work here was to develop an exoskeleton, called Harmony, with the goal of achieving advanced kinematic and dynamic characteristics for upper-body rehabilitation. In many previous exoskeleton designs, the shoulder mobility was simplified to that of a ball-and-socket joint. Some exoskeletons were designed to include the shoulder girdle mobility but limited to actively support the full shoulder mobility, including the coordinated movements of the shoulder girdle. Also, the quantitative evaluation of the kinematic compatibility between exoskeletons and the human body around the shoulder has been rarely reported. To fill the gap, we have designed a shoulder mechanism of the new kinematic structure that captures the full anatomic

shoulder mobility and a control scheme that can actively assist the SHR. The kinematic compatibility of the shoulder mechanism were quantified by measuring the residual forces in the interacting port during the coordinated shoulder movements. The results provide evidence of a good kinematic compatibility over a wide ROM, in addition to the users' feelings of unconstrained mobility.

Very few of the previous upper-body exoskeletons have employed force and impedance-oriented actuators. Accordingly, most upper-body exoskeletons are not able to provide force- and impedance-based therapeutic exercises and do not offer a very low impedance behavior that can encourage the user's voluntary free movements. We adopted the SEAs in Harmony and presented a control strategy with a exoskeleton dynamic model. The experimental results showed that Harmony exhibited very low impedance at both the joint and workspace level, imposing little resistance on the users' free movements. The desired workspace forces and impedances were realized with good accuracies.

The kinematic and dynamic features of Harmony will allow one to develop new therapeutic exercises with wide 3D anatomical movements and natural dynamic interactions, which have potential to increase the efficacy of robotic rehabilitation.

Harmony will be able to provide a variety of passive range exercises with natural shoulder mobility and a wide ROM that covers most ADLs. With the kinematic advantages, a joint-space impedance control will provide a safe interaction during passive range exercises.

A task-space force or impedance control in Harmony would provide effective task-oriented trainings. For example, trainings based on the assist-as-needed paradigm can be faithfully realized utilizing the dynamic transparency during the baseline control. The backdrivability of Harmony will encourage patients to move voluntarily as much as possible. Also, task-space forces against gravity acting on the center of masses of the human arm segments can be easily implemented to provide a gravity support for patients.

Nevertheless, some aspects of Harmony may need to improve. From a structural perspective, less room for a design modification is available when necessary. For example, when a higher load capacity is necessary for a variety of patient groups, the tight linkage design with the wide ROM specification of Harmony imposes restriction in implementing larger actuators. The load capacity may be increased by employing a lighter structural design and different material in the linkage or developing a new compact actuator. From the control perspective, advanced control schemes for the SEA may result in better torque control performance. For example, a full-state feedback based on the whole dynamics of the SEA or a control based on a disturbance observer may improve the torque responses (Kong et al., 2009; Paine et al., 2014), which will lead to better spatial force and impedance performances.

8. Conclusions

In this paper, we presented the kinematic design, modeling and control, and kinematic and dynamic evaluation of the upper-body exoskeleton, Harmony.

The design of the robot offers a good kinematic compatibility and a wide ROM that allow for composing a variety of unconstrained motions in rehabilitation exercises. With the torque-controllable actuators and the baseline control, the robot can produce task-space forces without a major distortion and a wide range of impedance. The baseline control enables the robot to be dynamically transparent to users' voluntary movements and allows for the development of control strategies by superposing the desired assistive force on it.

With the advanced features, the robot is expected to serve as a research platform for developing control strategies for upper-body robotic rehabilitation and investigating those clinical significances.

Funding

The author(s) disclosed receipt of the following financial support for the research, authorship, and/or publication of this article: This work was supported, in part, by the National Science Foundation (grant number 1157954).

References

Andreasen D, Aviles A, Allen S, et al. (2004) Exoskeleton for forearm pronation and supination rehabilitation. In: *International conference of the IEEE engineering in medicine and biology society*, San Francisco, CA, USA, 1–5 September 2004 vol. 1, pp.2714–2717. Piscataway, NJ: IEEE.

Ball SJ, Brown IE and Scott SH (2007) MEDARM: a rehabilitation robot with 5DOF at the shoulder complex. In: *IEEE/ASME international conference on advanced intelligent mechatronics*, Zurich, Switzerland, 4–7 September 2007, pp.1–6. Piscataway, NJ: IEEE.

Banala SK, Agrawal SK and Scholz JP (2007) Active Leg Exoskeleton (ALEX) for gait rehabilitation of motor-impaired patients. In: *IEEE 10th international conference on rehabilitation robotics*, Noordwijk, Netherlands, 13–15 June 2007, pp.401–407. Piscataway, NJ: IEEE.

Byl NN, Abrams GM, Pitsch E, et al. (2013) Chronic stroke survivors achieve comparable outcomes following virtual task specific repetitive training guided by a wearable robotic orthosis (UL-EXO7) and actual task specific repetitive training guided by a physical therapist. *Journal of Hand Therapy* 26(4): 343–352.

Carignan C, Liszka M and Roderick S (2005) Design of an arm exoskeleton with scapula motion for shoulder rehabilitation. In: *IEEE international conference on advanced robotics*, Seattle, WA, USA, 18–20 July 2005, pp.524–531. Piscataway, NJ: IEEE.

Cauraugh JH, Lodha N, Naik SK, et al. (2010) Bilateral movement training and stroke motor recovery progress: A structured review and meta-analysis. *Human Movement Science* 29(5): 853–870.

Centers for Disease Control and Prevention (2009) Prevalence and most common causes of disability among adults–united states,

2005. *MMWR: Morbidity and Mortality Weekly Report* 58(16): 421–426.

Chapel JD and Su R (1992) Coupled stability characteristics of nearly passive robots. In: *Proceedings of the 1992 IEEE international conference on robotics and automation*, Nice, France, 12–14 May 1992, pp.1342–1347. Piscataway, NJ: IEEE.

Colgate JE and Hogan N (1988) Robust control of dynamically interacting systems. *International Journal of Control* 48(1): 65–88.

Combs SA, Kelly SP, Barton R, et al. (2010) Effects of an intensive, task-specific rehabilitation program for individuals with chronic stroke: A case series. *Disability & Rehabilitation* 32(8): 669–678.

Conditt MA, Gandolfo F and Mussa-Ivaldi FA (1997) The motor system does not learn the dynamics of the arm by rote memorization of past experience. *Journal of Neurophysiology* 78(1): 554–560.

Dromerick AW, Edwards DF and Kumar A (2008) Hemiplegic shoulder pain syndrome: Frequency and characteristics during inpatient stroke rehabilitation. *Archives of Physical Medicine and Rehabilitation* 89(8): 1589–1593.

Edsinger-Gonzales A and Weber J (2004) Domo: A force sensing humanoid robot for manipulation research. In: *IEEE/RAS international conference on humanoid robots*, Santa Monica, CA, USA, 10–12 November 2004, vol. 1, pp.273–291. Piscataway, NJ: IEEE.

Ergin MA and Patoglu V (2012) ASSISTON-SE: A self-aligning shoulderelbow exoskeleton. In: *IEEE international conference on robotics and automation*, Saint Paul, MN, USA, 14–18 May 2012, pp.2479–2485. Piscataway, NJ: IEEE.

Featherstone R (1987) *Robot Dynamics Algorithms*. Dordrecht, The Netherlands: Kluwer Academic Publishers.

Featherstone R and Orin D (2000) Robot dynamics: equations and algorithms. In: *ICRA*, San Francisco, CA, USA, 24–28 April pp.826–834. Piscataway, NJ: IEEE.

Garrec P, Friconneau J, Measson Y, et al. (2008) ABLE, an innovative transparent exoskeleton for the upper-limb. In: *IEEE/RSJ international conference on intelligent robots and systems*, Nice, France, 22–26 September 2008, pp.1483–1488. Piscataway, NJ: IEEE.

Go AS, Mozaffarian D, Roger VL, et al. (2014) Heart disease and stroke statistics–2014 update: A report from the American heart association. *Circulation* 129(3): e28.

Hogan N (1985) Impedance control: An approach to manipulation: Part III Application. *Journal of Dynamic Systems, Measurement, and Control* 107(1): 17–24.

Hogan N (1989) Controlling impedance at the man/machine interface. In: *Proceedings of the 1989 IEEE international conference on robotics and automation*, Scottsdale, AZ, USA, 14–19 May 1989, pp.1626–1631. Piscataway, NJ: IEEE.

Hollerbach JM and Flash T (1982) Dynamic interactions between limb segments during planar arm movement. *Biological Cybernetics* 44(1): 67–77.

Jaraczewska E and Long C (2006) Kinesio® taping in stroke: improving functional use of the upper extremity in hemiplegia. *Topics in Stroke Rehabilitation* 13(3): 31–42.

Kahn LE, Lum PS, Rymer WZ, et al. (2006) Robot assisted movement training for the stroke-impaired arm: Does it matter what the robot does? *Journal of Rehabilitation Research and Development* 43(5): 619.

Kazerooni H (1987) Robust, non-linear impedance control for robot manipulators. In: *Proceedings of the 1987 IEEE international conference on robotics and automation*, Raleigh, NC, USA, 31 March3 April 1987 vol. 4, pp.741–750. Piscataway, NJ: IEEE.

Kim B, Rodot A and Deshpande AD (2014) Impedance control based on a position sensor in a rehabilitation robot. In: *ASME 2014 dynamic systems and control conference*, San Antonio, TX, 22–24 October 2014, V003T43A005. New York, NY: ASME. DOI: 10.1115/DSCC2014-6258

Kim B and Deshpande AD (2015) Controls for the shoulder mechanism of an upper-body exoskeleton for promoting scapulohumeral rhythm. In: *2015 IEEE international conference on rehabilitation robotics (ICORR)*, Singapore, 11–14 August 2015, pp.538–542. Piscataway, NJ: IEEE.

Klamroth-Marganska V, Blanco J, Campen K, et al. (2014) Three-dimensional, task-specific robot therapy of the arm after stroke: A multicentre, parallel-group randomised trial. *The Lancet Neurology* 13(2): 159–166.

Klein J, Spencer S, Allington J, et al. (2008) Biomimetic orthosis for the neurorehabilitation of the elbow and shoulder (BONES). In: *IEEE RAS & EMBS international conference on biomedical robotics and biomechatronics*, Scottsdale, AZ, USA, 19–22 October 2008, pp.535–541. Piscataway, NJ: IEEE.

Kong K, Bae J and Tomizuka M (2009) Control of rotary series elastic actuator for ideal force-mode actuation in human–robot interaction applications. *IEEE/ASME Transactions on Mechatronics* 14(1): 105–118.

Kong K, Moon H, Jeon D, et al. (2010) Control of an exoskeleton for realization of aquatic therapy effects. *IEEE/ASME Transactions on Mechatronics* 15(2): 191–200.

Krakauer JW (2006) Motor learning: Its relevance to stroke recovery and neurorehabilitation. *Current Opinion in Neurology* 19(1): 84–90.

Krebs HI and Hogan N (2006) Therapeutic robotics: A technology push. *Proceedings of the IEEE* 94(9): 1727–1738.

Krebs HI, Hogan N, Aisen ML, et al. (1998) Robot-aided neurorehabilitation. *IEEE Transactions on Rehabilitation Engineering* 6(1): 75–87.

Kwakkel G, Kollen BJ and Krebs HI (2008) Effects of robot-assisted therapy on upper limb recovery after stroke: a systematic review. *Neurorehabilitation and Neural Repair* 22: 111–121.

Lee TD, Swinnen SP and Serrien DJ (1994) Cognitive effort and motor learning. *Quest* 46(3): 328–344.

Levangie PK and Norkin CC (2011) Joint structure and function: a comprehensive analysis (2010) Robot assisted therapy for long-term upper-limb impairment after stroke. *New England Journal of Medicine* 362(19): 1772–1783.

Magermans D, Chadwick E, Veeger H, et al. (2005) Requirements for upper extremity motions during activities of daily living. *Clinical Biomechanics* 20(6): 591–599.

Milot MH, Spencer SJ, Chan V, et al. (2013) A crossover pilot study evaluating the functional outcomes of two different types of robotic movement training in chronic stroke survivors using the arm exoskeleton BONES. *Journal NeuroEngineering Rehabilitation* 10: 112.

Nef T, Guidali M and Riener R (2009) ARMin III–Arm therapy exoskeleton with an ergonomic shoulder actuation. *Applied Bionics and Biomechanics* 6(2): 127–142.

Paine N, Oh S and Sentis L (2014) Design and control considerations for high-performance series elastic actuators. *IEEE/ASME Transactions on Mechatronics* 19(3): 1080–1091.

Patton JL, Stoykov ME, Kovic M, et al. (2006) Evaluation of robotic training forces that either enhance or reduce error in chronic hemiparetic stroke survivors. *Experimental Brain Research* 168(3): 368–383.

Paul RP (1981) *Robot Manipulators: Mathematics, Programming, and Control: The Computer Control of Robot Manipulators*. Cambridge, MA: MIT Press.

Perry JC, Rosen J and Burns S (2007) Upper-limb powered exoskeleton design. *IEEE/ASME Transactions on Mechatronics* 12(4): 408–417.

Prange GB, Jannink MJ, Groothuis-Oudshoorn CG, et al. (2006) Systematic review of the effect of robot-aided therapy on recovery of the hemiparetic arm after stroke. *Journal of Rehabilitation Research and Development* 43(2): 171.

Pratt G, Williamson MM, et al (1995) Series elastic actuators. In: *Proceedings of the 1995 IEEE/RSJ international conference on intelligent robots and systems 95, 'human robot interaction and cooperative robots'*, Pittsburgh, PA, 5–9 August 1995, vol. 1, pp.399–406. IEEE. Piscataway, NJ: IEEE.

Ren Y, Park HS and Zhang LQ (2009) Developing a whole-arm exoskeleton robot with hand opening and closing mechanism for upper limb stroke rehabilitation. In: *IEEE international conference on rehabilitation robotics*, Kyoto, Japan, 23–26 June 2009, pp.761–765. Piscataway, NJ: IEEE.

Rijntjes M, Haevernick K, Barzel A, et al. (2009) Repeat therapy for chronic motor stroke: a pilot study for feasibility and efficacy. *Neurorehabilitation and Neural Repair* 23: 275–280.

Roberts RK, Paul R and Hillberry BM (1985) The effect of wrist force sensor stiffness on the control of robot manipulators. In: *Proceedings of the 1985 IEEE international conference on robotics and automation*, St. Louis, MO, USA, 25–28 March 1985, vol. 2, pp.269–274. Piscataway, NJ: IEEE.

Sanchez R Jr, Wolbrecht E, Smith R, et al. (2005) A pneumatic robot for retraining arm movement after stroke: Rationale and mechanical design. In: *Proceedings IEEE international conference on rehabilitation robotics*, Chicago, IL, USA, 28 June–1 July 2005, pp.500–504. Piscataway, NJ: IEEE.

Schiele A and van der Helm FC (2006) Kinematic design to improve ergonomics in human machine interaction. *IEEE Transactions on Neural Systems and Rehabilitation Engineering* 14(4): 456–469.

Schmidt RA and Lee T (1988) *Motor Control and Learning: A Behavioral Emphasis*. Champaign, IL: Human Kinetics.

Slotine JJE, Li W, et al (1991) *Applied Nonlinear Control*. Vol. 199. Englewood Cliffs, NJ: Prentice-Hall.

Stewart KC, Cauraugh JH and Summers JJ (2006) Bilateral movement training and stroke rehabilitation: A systematic review and metaanalysis. *Journal of the Neurological Sciences* 244(1): 89–95.

Stienen AH, Hekman EE, Van Der Helm FC, et al. (2009) Self-aligning exoskeleton axes through decoupling of joint rotations and translations. *IEEE Transactions on Robotics* 25(3): 628–633.

Taal SR and Sankai Y (2011) Exoskeletal spine and shoulder girdle for full body exoskeletons with human versatility. In: *2011 IEEE international conference on robotics and automation (ICRA)*, Shanghai, China, 9–13 May 2011, pp.2217–2222. Piscataway, NJ: IEEE.

Tsagarakis NG and Caldwell DG (2003) Development and control of a soft-actuated exoskeleton for use in physiotherapy and training. *Autonomous Robots* 15(1): 21–33.

Vallery H, Veneman J, Asseldonk EV, et al. (2008) Compliant actuation of rehabilitation robots. *IEEE Robotics & Automation Magazine* 15(3): 60–69.

Vertechy R, Frisoli A, Dettori A, et al. (2009) Development of a new exoskeleton for upper limb rehabilitation. In: *Proceedings IEEE international conference on rehabilitation robotics*, Kyoto, Japan, 23–26 June 2009, pp.188–193. Piscataway, NJ: IEEE.

Volpe BT, Krebs HI and Hogan N (2001) Is robot-aided sensorimotor training in stroke rehabilitation a realistic option? *Current Opinion in Neurology* 14(6): 745–752.

Waller SM and Whitall J (2008) Bilateral arm training: why and who benefits? *NeuroRehabilitation* 23(1): 29–41.

Whitall J, Waller SM, Silver KH, et al. (2000) Repetitive bilateral arm training with rhythmic auditory cueing improves motor function in chronic hemiparetic stroke. *Stroke* 31(10): 2390–2395.

Wing K, Lynskey JV and Bosch PR (2008) Whole-body intensive rehabilitation is feasible and effective in chronic stroke survivors: a retrospective data analysis. *Topics in Stroke Rehabilitation* 15(3): 247–255.

Zinn M, Roth B, Khatib O, et al. (2004) A new actuation approach for human friendly robot design. *The International Journal of Robotics Research* 23(4–5): 379–398.

Appendix 1: Index to multimedia extensions

The multimedia extension page is found at http://www.ijrr.org

Table of multimedia extensions.

Extension	Type	Description
1	Video	Mobility, range of motion, and impedance behaviors

Appendix 2: Passivity formalism with a dual-port interaction

Since each robot arm is attached to the human arm through two interacting ports at the upper arm and the wrist, passivity formalism for such a dual-port system is described here based on energy conservation (Slotine et al., 1991). We assume that the robot and human have a rigid connection. Although the connection at the interaction port, in reality, is compliant due to the flesh and cuffs, the assumption of a rigid connection is valid for the proof of passivity of the human–robot coupled system (Hogan, 1989). This is because the compliance in the interacting port can be safely assumed to be passive, so omitting it makes the coupled stability analysis more conservative. Figure 27 shows the input–output connectivity of two subsystems interacting with each other at two ports in feedback combination. The power balances of subsystems A and B are expressed as

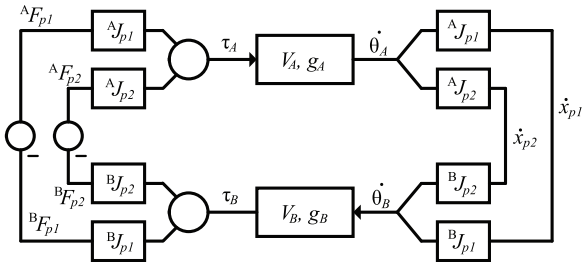

Fig. 27. Input–output connectivity of two multi-body articulated subsystems interacting with each other at two ports. For example, subsystems 'A' and 'B' are the arms of the human and robot, and ports 'p1' and 'p2' are the physical connections in the cuffs at the upper arm and the wrist, respectively.

$$\dot{V}_A = \dot{\theta}_A{}^{\mathrm{T}} \tau_A - g_A \tag{33}$$

$$\dot{V}_B = \dot{\theta}_B{}^{\mathrm{T}} \tau_B - g_B \tag{34}$$

where $\dot{V}_A$ and $\dot{V}_B$ are the time derivatives of the stored energy of subsystems A and B, where the storage functions are positive. $\dot{\theta}$ and τ with subscriptions are the joint velocity and torque vectors of the corresponding subsystems, and the multiplication of two vectors indicates external power input to each subsystem. g_A and g_B are positive scalar functions indicating internal power generation. The joint torque vectors are the sum of two interaction forces transformed by corresponding Jacobians

$$\tau_A = {}^{A}J_{p1}^{\mathrm{T}}\,{}^{A}F_{p1} + {}^{A}J_{p2}^{\mathrm{T}}\,{}^{A}F_{p2} \tag{35}$$

$$\tau_B = {}^{B}J_{p1}^{\mathrm{T}}\,{}^{B}F_{p1} + {}^{B}J_{p2}^{\mathrm{T}}\,{}^{B}F_{p2} \tag{36}$$

${}^{S}J_{pi}$ is the Jacobian of subsystem 'S' at port 'pi'. ${}^{S}F_{pi}$ is the force applied to subsystem 'S' from interaction port 'pi', having action–reaction pairs as

$${}^{A}F_{p1} = -{}^{B}F_{p1} \tag{37}$$

$${}^{A}F_{p2} = -{}^{B}F_{p2} \tag{38}$$

The velocities of the ports are commonly shared by two subsystems, converting to joint velocities of two subsystems separately as

$$\dot{x}_p 1 = {}^{A}J_{p1}\dot{\theta}_A = {}^{B}J_{p1}\dot{\theta}_B \tag{39}$$

$$\dot{x}_p 2 = {}^{A}J_{p2}\dot{\theta}_A = {}^{B}J_{p2}\dot{\theta}_B \tag{40}$$

Using equations (35)–(40), the sum of power balances of the two subsystems with the coupled system is shown to be dissipative as follows

$$\begin{aligned}
&\dot{V}_A + \dot{V}_B = \dot{\theta}_A{}^{\mathrm{T}}\tau_A + \dot{\theta}_B{}^{\mathrm{T}}\tau_B - (g_A + g_B) \\
&= \left({}^{A}J_{p1}^{+}\dot{x}_{p1}\right)^{\mathrm{T}A} J_{p1}^{\mathrm{T}\,A}F_{p1} + \left({}^{A}J_{p2}^{+}\dot{x}_{p2}\right)^{\mathrm{T}A} J_{p2}^{\mathrm{T}\,A}F_{p2} \\
&+ \left({}^{B}J_{p1}^{+}\dot{x}_{p1}\right)^{\mathrm{T}B} J_{p1}^{\mathrm{T}\,B}F_{p1} + \left({}^{B}J_{p2}^{+}\dot{x}_{p2}\right)^{\mathrm{T}B} J_{p2}^{\mathrm{T}\,B}F_{p2} \\
&- (g_A + g_B) \\
&= \dot{x}_{p1}{}^{\mathrm{T}A}F_{p1} + \dot{x}_{p2}{}^{\mathrm{T}A}F_{p2} + \dot{x}_{p1}{}^{\mathrm{T}B}F_{p1} + \dot{x}_{p2}{}^{\mathrm{T}B}F_{p2} \\
&- (g_A + g_B) \\
&= -(g_A + g_B)
\end{aligned} \tag{41}$$

where J^{+} indicates the pseudoinverse $((J^{\mathrm{T}}J)^{-1}J^{\mathrm{T}})$ of each Jacobian. Having only the dissipative terms, the feedback combination of the two subsystems interacting with each other at the two ports holds for passivity formalism.